

The AGEL Survey Data Release 2: A Gravitational Lens Sample for Galaxy Evolution and Cosmology

TANIA M. BARONE,^{1, 2} KEERTHI VASAN G.C.,^{3, 4} KIM-VY TRAN,^{5, 2} GLENN G. KACPRZAK,^{1, 2} KARL GLAZEBROOK,^{1, 2}
 TUCKER JONES,³ DUNCAN J. BOWDEN,^{5, 6} FAITH DALESSANDRO,³ NANDINI SAHU,^{7, 2} HANNAH SKOBE,⁸
 REBECCA J. ALLEN,¹ A. MAKAI BAKER,⁹ DANIEL J. BALLARD,¹⁰ YUGUANG CHEN,^{3, 11} THOMAS E. COLLETT,¹²
 GIOVANNI FERRAMI,^{13, 2} JIMENA GONZÁLEZ,¹⁴ WILLIAM GOTTEMOLLER,⁵ ANISHYA HARSHAN,¹⁵ XIAOSHENG HUANG,^{16, 17}
 LEENA IWAMOTO,⁵ COLIN JACOBS,^{1, 2} TESLA E. JELTEMA,^{18, 19} KAUSTUBH RAJESH GUPTA,¹ GERAINT F. LEWIS,¹⁰
 SEBASTIAN LOPEZ,²⁰ THEMİYA NANAYAKKARA,^{1, 2} NIKOLE M. NIELSEN,^{21, 1, 2} JACKSON O'DONNELL,^{18, 19} HUIMIN QU,¹⁰
 SUNNY RHOADES,³ ANOWAR SHAJIB,^{22, 23} SARAH M. SWEET,^{24, 2} AND NICOLAS TEJOS²⁵

¹Centre for Astrophysics and Supercomputing, Swinburne University of Technology, PO Box 218, Hawthorn, VIC 3122, Australia

²The ARC Centre of Excellence for All Sky Astrophysics in 3 Dimensions (ASTRO 3D), Australia

³Department of Physics and Astronomy, University of California, Davis, 1 Shields Avenue, Davis, CA 95616, USA

⁴The Observatories of the Carnegie Institution for Science, 813 Santa Barbara Street, Pasadena, CA 91101, USA

⁵Center for Astrophysics, Harvard & Smithsonian, Cambridge, MA 02138, USA

⁶School of Physics & Astronomy, University of Southampton, Southampton SO17 1BJ, UK

⁷University of New South Wales, Sydney, NSW 2052, Australia

⁸Department of Physics, McWilliams Center for Cosmology and Astrophysics, Carnegie Mellon University, 5000 Forbes Avenue, Pittsburgh, PA 15213, USA

⁹School of Physics and Astronomy, Monash University, Clayton VIC 3800, Australia

¹⁰Sydney Institute for Astronomy, School of Physics, A28, The University of Sydney, NSW 2006, Australia

¹¹Department of Physics, The Chinese University of Hong Kong, Shatin, N.T., Hong Kong SAR, China

¹²Institute of Cosmology and Gravitation, University of Portsmouth, Burnaby Rd, Portsmouth PO1 3FX, UK

¹³School of Physics, University of Melbourne, Parkville, VIC 3010, Australia

¹⁴Physics Department, University of Wisconsin-Madison. 2320 Chamberlin Hall. Madison, WI 53706-1390, USA

¹⁵University of Ljubljana, Department of Mathematics and Physics, Jadranska ulica 19, SI-1000 Ljubljana, Slovenia

¹⁶Department of Physics & Astronomy, University of San Francisco, 2130 Fulton Street, San Francisco, CA 94117-1080, USA

¹⁷4 Physics Division, Lawrence Berkeley National Laboratory, 1 Cyclotron Road, Berkeley, CA 94720, USA

¹⁸University of California, Santa Cruz, Santa Cruz, CA 95064, USA

¹⁹Santa Cruz Institute for Particle Physics, Santa Cruz, CA 95064, USA

²⁰Departamento de Astronomía, Universidad de Chile, Casilla 36-D, Santiago, Chile

²¹Homer L. Dodge Department of Physics and Astronomy, The University of Oklahoma, 440 W. Brooks St., Norman, OK 73019, USA

²²Department of Astronomy & Astrophysics, University of Chicago, Chicago, IL 60637, USA

²³Kavli Institute for Cosmological Physics, University of Chicago, Chicago, IL 60637, USA

²⁴School of Mathematics and Physics, University of Queensland, Brisbane, QLD 4072, Australia

²⁵Instituto de Física, Pontificia Universidad Católica de Valparaíso, Casilla 4059, Valparaíso, Chile

ABSTRACT

The ASTRO 3D Galaxy Evolution with Lenses (AGEL) Survey is an ongoing effort to spectroscopically confirm a diverse sample of gravitational lenses with high spatial resolution imaging, to facilitate a broad range of science outcomes. The AGEL systems span single galaxy-scale deflectors to groups and clusters, and include rare targets such as galaxy-scale lenses with multiple sources, lensed quiescent galaxies, and Einstein rings. We build on the 77 systems presented in Tran et al. 2022 (AGEL data release 1) to present a total 138 lenses, and high resolution F140W and F200LP Hubble Space Telescope images for 71 lenses from a completed HST SNAP program. Lens candidates were originally identified by convolutional neural networks in the DES and DECaLS imaging fields, and of the targets with follow-up spectroscopy we find a high (96 %) success rate. Compared with other spectroscopic lens samples, AGEL lenses tend to have both higher redshift deflectors and sources. We briefly discuss the common causes of false-positive candidates, and strategies for mitigating false-positives in next

generation lens searches. Lastly, we present 6 galaxy-scale double-source plane lenses useful for cosmological analyses. With next-generation telescopes and surveys such as Euclid, Vera Rubin’s Legacy Survey of Space and Time, Keck Observatory’s KAPA program, and 4MOST’s 4SLSLS surveys on the horizon, the AGEL survey represents a pathfinder for refining automated candidate search methods and identifying and triaging candidates for followup based on scientific potential.

Keywords: Gravitational lensing(670) — Galaxy evolution(594) — Cosmology(343) — Redshift surveys(1378)

1. INTRODUCTION

Strong gravitational lenses are powerful tools to study the most elusive aspects of our Universe. The lensing configuration and magnification of the background source depends upon (i) the total mass distribution of the foreground lens (the ‘deflector’) which range from individual galaxies to clusters, and (ii) the geometry of the universe in the angular diameter distances between us, the deflector, and the source. As a result strong gravitational lenses are used to explore a broad range of astrophysical phenomena in both the lensed source and the foreground deflector, as well as other targets along the line of sight and the cosmological nature of our Universe.

With the deflectors acting as cosmic-scale magnifying glasses, the bright and highly magnified source galaxies offer a rare view of early galaxy formation and evolution at high-redshift ($z > 1$; e.g. Zheng et al. 2012; McLeod et al. 2015; Zhuang et al. 2023; Keerthi Vasan et al. 2023) yielding high spatial resolutions (sub-kpc scales) out of reach for even the most powerful telescopes (e.g. Ritondale et al. 2019). Source magnifications (μ) of over an order of magnitude are commonly reached by galaxy-scale lenses (Shu et al. 2016a), while lensing by clusters can reach magnifications of $\mu = 10 - 100$ (Yuan et al. 2012; Coe et al. 2013; Atek et al. 2015; Ebeling et al. 2018; Florian et al. 2021; Sharon et al. 2022; Bergamini et al. 2023; Price et al. 2024).

Lensing is sensitive to all mass along the line of sight, so strong lenses provide a way to probe the distribution of both dark and baryonic matter in the deflector. The total mass density profile of massive quiescent galaxies reflects their formation history, with the slope of the profile evolving with redshift due to the two-phases of their formation: mass growth driven by in-situ star formation at high redshift, followed by mass growth through mergers (Oser et al. 2010). Therefore the evolution with redshift of quiescent galaxy total mass density profiles is a key probe of galaxy evolution (e.g. Ruff et al. 2011; Bolton et al. 2012; Sonnenfeld et al. 2013b; Remus et al. 2017; Wang et al. 2019; Sahu et al. 2024).

In addition to the dark and baryonic matter within the galaxy, the faint diffuse gas surrounding line of sight galaxies in their circumgalactic mediums leaves absorption signatures in the spectrum of the brightly lensed background sources (e.g. Zahedy et al. 2016; Lopez et al. 2020; Mortensen et al. 2021). With precise lens modelling of high resolution imaging, the spatial distribution of diffuse circumgalactic gas can also be measured from its gravitational effect (Barone et al. 2024).

From precision lens models we can also search for and constrain the scale of dark matter substructure. Dark matter subhalos along the line of sight lead to subtle perturbations in the resulting lens configuration, which can be detected with precise lens modelling on high spatial resolution imaging. Both warm and cold dark matter models predict that galaxies should contain thousands of dark matter subhalos, with Λ CDM predicting a higher abundance of low-mass halos than warmer models (Bode et al. 2001). Therefore detections at low halo masses will allow us to distinguish between theoretical dark matter models (e.g. Vegetti et al. 2012; Nightingale et al. 2022; Lagattuta et al. 2023; Bayer et al. 2023; Hughes et al. 2024).

Lastly, gravitational lenses can also be used to infer the geometry and composition of the Universe at large scales. The time delay between multiply lensed images of variable sources such as supernovae (Refsdal 1964; Goobar et al. 2002; More et al. 2017; Bayer et al. 2021) and quasars (e.g. Suyu et al. 2010; Wong et al. 2020) is sensitive to the Hubble constant H_0 , providing an additional measurement of H_0 independent from the distance ladder and the cosmic microwave background (CMB). Other cosmological parameters including the dark energy equation of state w can be measured from lenses with multiple sources (Collett & Auger 2014; Caminha et al. 2022). This method, termed gravitational lens cosmography (Blandford & Narayan 1992; Treu 2010), also provides constraints on the total matter density of the Universe, Ω_m , and the curvature, Ω_k , that are nearly orthogonal to those from the CMB and baryon acoustic oscillations (Eisenstein et al. 2005; Percival et al. 2010), proving these methods to be highly complimentary.

1.1. Lens surveys

The difficulty in many of these science areas is the limited samples of high quality spectroscopically confirmed lenses. Bright ($R_{AB} \leq 22$ mag) systems are rare ($\lesssim 0.1$ per square degree; Jacobs et al. 2019a,b; Huang et al. 2020), and therefore discovering new lenses requires wide area imaging over 100s of square degrees. Confirming strong gravitational lenses often requires both high resolution subarcsecond imaging and spectroscopy. Therefore, although simulations predict order $\sim 10^3$ more galaxy-galaxy lenses should be detectable in currently available wide-field imaging surveys (Collett 2015), the number of spectroscopically confirmed lenses is far smaller (few 100s).

The first generation of dedicated lens searches in wide-field imaging surveys was made possible by SDSS (the Sloan Digital Sky Survey; York et al. 2000). SLACS (Sloan Lens ACS Survey; Bolton et al. 2008) and BELLS (BOSS Emission-Line Lens Survey; Brownstein et al. 2012) confirmed first 70 then another 36 lenses in SDSS, identified by searching for high redshift emission lines within the fibre spectroscopy of a lower redshift target. While this method had the advantage of immediate spectroscopic redshift confirmation, only systems with small Einstein radii (smaller than the diameter of the fiber, so $R_E < 1.5''$ for SLACS and $R_E < 1''$ for BELLS) were captured and galaxy-scale lenses with larger Einstein radii and group or cluster lenses were missed.

Imaging has proven to be a powerful and complementary method of identifying lens candidates. Early searches for cluster-scale lenses relied on visual identification, such as SGAS (the Sloan Giant Arc Survey; Hennawi et al. 2008; Sharon et al. 2020). However finding galaxy and group-scale lenses requires search methods that can be easily scaled to large datasets. As a result, teams began using dedicated algorithms to search for blue arcs around massive red foreground galaxies in large imaging surveys. The CASSOWARY survey (the CAmbridge Sloan Survey Of Wide ARcs in the skY; Stark et al. 2013) used SDSS imaging to search for blue sources within a specified separation from luminous red galaxies (Belokurov et al. 2009). Their search yielded 45 objects, including now well known lenses such as the Cosmic Horseshoe (Belokurov et al. 2007). The SL2S team (the Strong Lensing Legacy Survey; Cabanac et al. 2007) developed this technique further and used separate algorithms optimised to search for giant arcs around groups and clusters (More et al. 2012, using ARCFINDER; Alard 2006) and for galaxy-scale lens (Gavazzi et al. 2012, using RINGFINDER; Gavazzi et al. 2014) in the CFHT (Canada-France-Hawaii Telescope) Survey. Although these methods led to many successful identifi-

cations, due to their prescriptive nature, they can only find systems that fit the tight search parameters. As a result, systems with red sources (due either to dust or their quiescent nature) are disfavoured, as well as systems with small, truncated arcs.

As wide-field area surveys have improved (in depth and breadth) and the demand for larger and more diverse lens samples increased, lens candidate searches are now relying on sophisticated machine learning methods, specifically convolutional neural networks (CNNs; Le-Cun et al. 1989), to sort through the terabytes of images to find the 1 in $\sim 100,000$ galaxies that is strongly lensed (Jacobs et al. 2019b). CNNs have been successfully applied to the CFHTLS (Jacobs et al. 2017), KiDS (Petrillo et al. 2017, 2019; Li et al. 2020), DES (Jacobs et al. 2019a,b), PanSTARRS (Cañameras et al. 2020) and DECaLS (Huang et al. 2020, 2021) imaging surveys, returning thousands of new lens candidates. The CNN approach has proven to be highly successful in producing high-fidelity candidate samples that were missed by previous searches despite being comparably bright (Tran et al. 2022).

Over the next decade approximately $\sim 10^6$ galaxy-galaxy strong lenses will be discovered by cosmological surveys such as Euclid and the Legacy Survey of Space and Time (Collett 2015), a two orders of magnitude increase in the number of lens candidates currently known and a three orders of magnitude increase over the hundreds of systems that are currently spectroscopically confirmed (Bolton et al. 2008; Sonnenfeld et al. 2013a; Bolton et al. 2012; Shu et al. 2016b). In this coming era, it will become even more important to hone and refine lens search methods.

While coming surveys will provide a plethora of lens images, for many science cases spectroscopic confirmation and redshift measurement is still a crucial requirement. The future 4MOST (4 meter Multi-Object Spectroscopic Telescope) facility will obtain spectra for $\sim 10^4$ of these lenses via 4SLSLS (The 4MOST Strong Lensing Spectroscopic Legacy Survey; Collett et al. 2023), however that represents only 1% of the total candidate sample. Furthermore, similarly for SLACS and BELLS, only targets with Einstein radii smaller than the fiber (radius = $0.725''$) will the spectrum capture both the source and deflector light. Importantly, because lenses are so sparse across the sky, 4SLSLS will be sharing the focal plane of 4MOST with other surveys and as a result target choice is limited. Therefore dedicated spectroscopy of high-value targets will still be required.

1.2. The ASTRO3D Galaxy Evolution with Lenses Survey

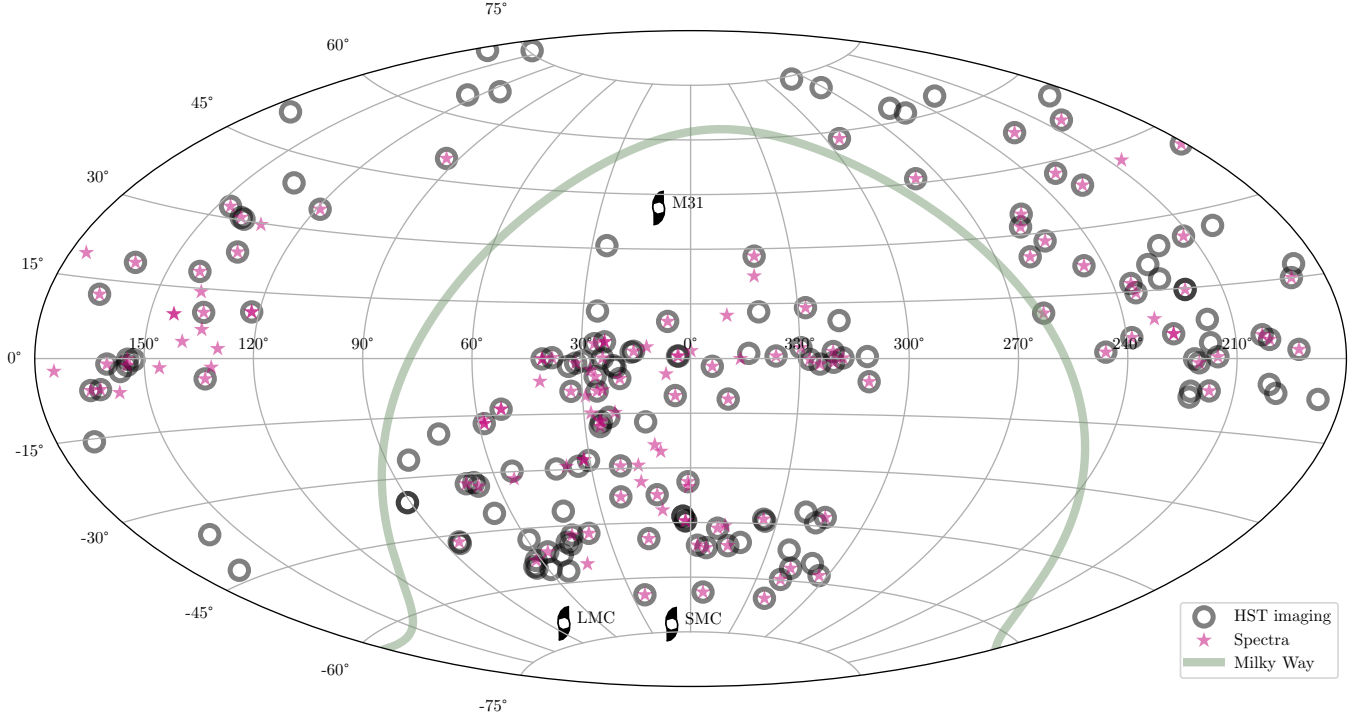


Figure 1. Sky location of targets with spectroscopic follow-up (magenta stars) and HST imaging (black circles) from programs 16773 (PI Glazebrook), 17307 (PI Tran) and 15867 (PI Huang). The plane of the Milky Way is shown in green. The Large and Small Magellanic Clouds and M31 are shown by black swirl symbols.

The goal of the ASTRO 3D Galaxy Evolution with Lenses (AGEL) Survey (Tran et al. 2022) is to spectroscopically confirm a diverse range of candidate lenses to enable a diverse range of science. In the first AGEL data release (Tran et al. 2022) we published a catalogue of 104 new redshifts in a total 68 systems. Combined with literature redshifts, we presented 53 lens systems with deflector and source redshifts, and 15 systems with either a source or deflector spectroscopic redshift. In this second release we present an additional 106 new redshifts in a total 138 systems. Combined with literature redshifts, 101 targets have both source and deflector redshifts, 32 have just a source redshift and 5 systems have only a deflector redshift.

In addition to the expanded spectroscopic catalogue we present 111 high resolution HST images as part of 2 programs (16773 PI Glazebrook, 17307 PI Tran), as well as an additional 51 images from literature program 15867 (PI Huang; Huang et al. 2025).

Targets span the full range of right ascensions and have declinations ranging between $-65^\circ < \delta < 75^\circ$; the sky distribution of targets is shown in Figure 1. Candidate lenses were primarily chosen from Jacobs et al. (2019a,b) but also include targets from Huang et al. (2020, 2021) and Diehl et al. (2017). Systems are named

by their right ascension and declination with a letter A, B, C, differentiating between multiple sources.

The paper is structured as follows. In Section 2 we present the 111 HST images and 51 literature images. We then summarise the observations used for measuring redshifts including the various instrument setups and present the redshift catalogue in Tables 4 and 5. In Section 4 we discuss the sample characteristics: firstly discussing false-positives lens candidates in 4.1, followed by a comparison of the AGEL redshift distribution to other lensing surveys and expectations from an analytical model in 4.2. Lastly in Section 4.3 we present galaxy-scale lenses we have found that have multiple source planes. All magnitudes are AB magnitudes. We assume a flat Λ cold dark matter (Λ CDM) Universe with $\Omega_\Lambda = 0.7$, $\Omega_M = 0.3$, and $H_0 = 70\text{km s}^{-1}\text{Mpc}^{-1}$. Redshifts are quoted with respect to the solar system's barycenter.

2. HIGH RESOLUTION HST IMAGING

As part of the survey we have obtained two HST imaging programs: a completed SNAP (ID: 16773, PI: Glazebrook, cycles 29-30, see Figure 3) awarded 150 orbits with WFC3 and an ongoing GAP program (ID: 17307, PI: Tran, cycles 32-37, see Figure 4) awarded 500 orbits with ACS. The goal of these programs is to build a legacy library of bright strong gravitational lenses

AGEL Name (1)	HST object name (2)	Comment (3)
Program 16773, PI Glazebrook		
AGEL211515+101153A	DCLS2115+1011	Not a lens: ring galaxy
AGEL224400+124540A	DCLS2244+1245	Not a lens: blue blob adjacent to red star
AGEL131330-064211A	DCLS1313-0642	Not a lens: blue blobs adjacent to red galaxy
AGEL132557+263659A	DCLS1325+2636	Not a lens: blue blobs adjacent to red galaxy
AGEL105100-055628A	DLS432021848	Guiding issue: no usable UVIS data
AGEL140839+253104A	DCLS1408+2531	Guiding issue: lost UVIS data from first visit but was revisited
AGEL001030-431515A	DESJ0010-4315	Guiding issue: has only a single useable IR exposure
AGEL022709-471856A	DESJ0227-4718	Used original observing strategy
AGEL025029-410418A	DESJ0250-4104	Used original observing strategy
AGEL034131-513045A	DESJ0341-5130	Used original observing strategy
AGEL035346-170639A	DCLS0353-1706	Used original observing strategy
AGEL032904-565658A	DESJ0329-5656	Used original observing strategy
AGEL013355-643413A	DESJ0133-6434	Used original observing strategy
Program 17307, PI Tran		
AGEL180556+705719A	DESI-271.4849+70.9553	No usable data
AGEL033631-295144A	DES0337-295	No usable data
AGEL014556+040229A	DESJ0145+0402	incorrect sky coordinates target not observed
Program 15867, PI Huang		
AGEL103255+751854A	DESI-158.2306+75.3149	No usable data
AGEL142822+031800A	DESI-217.0936+03.3000	No usable data
AGEL085331+232155A	DESI-133.3800+23.3652	Some usable data

Table 1. Details of targets with data issues from HST programs 16773, 17307, and 15867. (1) AGEL object name, (2) object name used in the HST observations, (3) target details.

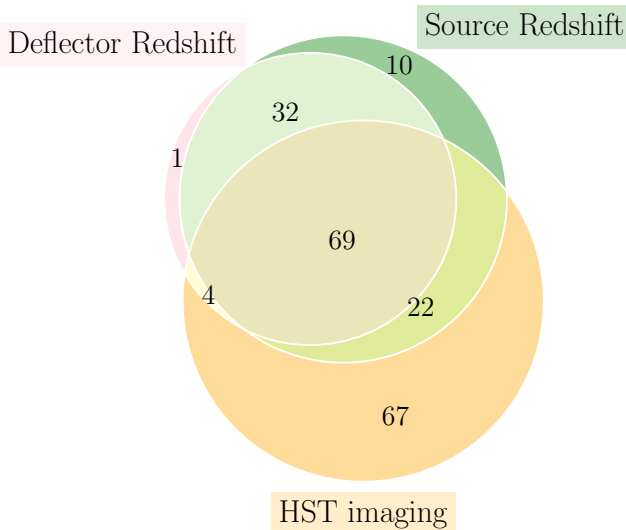


Figure 2. Venn diagram of targets with source redshifts, deflector redshifts, and HST imaging from completed AGEL large program 16773 (PI: Glazebrook), ongoing AGEL large program 17307 (PI: Tran) and archival SNAP program targeting gravitational lenses 15867 (PI: Huang).

that span galaxy to cluster-scale halos. Given the resolution of HST’s WFC3 and ACS (point spread func-

tions of $0.124 - 0.156''$, $0.083 - 0.089''$ and $0.1 - 0.14$ for WFC3/IR, WFC3/UVIS, and ACS/WCF respectively), HST has a distinct advantage for determining accurate lens models over ground-based surveys such as DES, HSC, and the upcoming LSST, as well as space-based imaging surveys with Euclid and Roman (both $0.1''/\text{pixel}$). If we consider these two programs as well as imaging from archival SNAP program 15867 (PI: Huang) a total of 69 targets have the full combination of source redshift, deflector redshift, and HST imaging (see Figure 2).

One of the primary motivations for the high-resolution follow-up imaging is to enable reliable lens models, which are necessary to access the full scope of science from lenses. The precision on the magnification inferred from lens models on ground-based imaging can be improved 10-fold with HST imaging (cf. $\mu = 77^{+43}_{-26}$ from Sukay et al. (2022) to $\mu = 14.6^{+0.55}_{-1.07}$ from Zhuang et al. (2023) for the same system). Precise measurements of the lensing magnification are needed to constrain source properties such as the stellar mass and star formation rate. Furthermore, high resolution imaging helps confirm the lensing nature of the target and the multiplicity and morphology of the lensed source. Thus far, AGEL

targets ranging from galaxy to group and cluster scale lenses have been modelled thanks to this new HST imaging (Zhuang et al. 2023; Sahu et al. 2024; Sheu et al. 2024). While all SNAP and GAP data has zero propriety period and so the raw data is all publicly available, we provide reduced files as well as RGB images on the AGEL Survey website¹.

While not all targets in the AGEL spectroscopic catalogue have HST imaging, all targets have *grz* imaging from the Dark Energy Survey (DES; Abbott et al. 2018) and the The Dark Energy Camera Legacy Survey (DECaLS; Dey et al. 2019) by virtue of the selection method (see Section 3). The DES and DECaLS survey span 9000 deg² and reaches 5 σ depths of $g = 24.0$, $r = 23.4$ and $z = 22.5$ mags.

2.1. WFC3 SNAP Program 16773, PI Glazebrook

The completed program 16773 obtained WFC3 UVIS/F200LP and IR/F140W imaging and was scheduled 76 visits of the total 150 orbits, (51%), representing a high visit rate for HST SNAP programs (completion rates for SNAP programs on WFC3 are typically 18%²). This high completion rate is attributed to two key factors which maximised the programs schedulability, (i) all sky targets, and (ii) visit durations under 30 minutes. Of those 76 visits, 75 objects were targeted. 2 targets have been spectroscopically confirmed to not be lenses, and 2 other targets are unlikely to be lenses based on their HST imaging. A further 3 targets were affected by guiding issues resulting in partial data loss, however at least one exposure in one band is available. See Table 1 for details of these targets. The final tally for the program is therefore 71 lenses, of which 50 also have spectroscopy (source or deflector or both). We show all 71 lenses in Figure 3.

The observing strategy started with 3×300s in F140W followed by 300s in F200LP. To facilitate better cosmic ray rejection in the F200LP images, and based on the analysis of Shajib et al. (2022) we later updated this strategy to 3×200s for F140W and 2×300s for F200LP. 6 targets were observed using the initial strategy, the rest were observed using the updated exposure times (see Table 1). We reduced the images using STScI DrizzlePac to align exposures, correct for background distortion, and remove flagged cosmic rays. To create the combined images, we adjusted the rotation of the stacked image to be in the same orientation across filters. A pixel size of 0.08'' was set to match F200LP to the scaling of F140W.

The F140W filter was chosen to optimise the target S/N, thereby decreasing the exposure time required for lens confirmation. Assuming a $10^8 M_\odot$ source at $z = 2$ with a young stellar population lensed with a magnification of $\mu = 10$ would result in an H(AB)=26 (Tomczak et al. 2014), which are on the scale of massive star-forming clumps. Depending upon the shape of the spectral energy distribution (SED) the S/N in optical bands will be similar to or less than in the IR channel. For such star-forming sources at $1 < z < 3.5$ with flat SEDs the optical wavelength S/N will be similar, but in instances of reddening due to dust, old stellar population age, or high redshift the IR channel will have a higher S/N. Based on the 3×200s for F140W and 2×300s for F200LP observing strategy used for the majority of the observations, we obtained 5 σ limiting surface brightnesses of 21.8 and 26.4 mag/arcsec in the F140W and F200LP filters respectively.

To cleanly distinguish between source light and foreground/or deflector light it is important to have colour information (Metcalf et al. 2019). In particular, cleanly identifying source counter images is critical for robust lens modelling. Therefore each target was also observed in the wide F200LP filter, which was chosen to maximise S/N and to probe the rest-frame ultraviolet.

2.2. ACS GAP Program 17307, PIs Tran and Shajib

Program 17307 is a (presently ongoing) imaging campaign with ACS in the F606W filter. GAP programs with ACS were introduced by STScI to make use of orbits in which GO and SNAP targets cannot be scheduled. GAP programs therefore require all-sky targets and visit durations of $\lesssim 25$ minutes, and in the past have run for 5 years (compared with SNAP programs which run for 2 years). To increase the schedulability of the observations we use short exposure times of 2×337 s per target. Between the start of observations (November 2023) until the end of 2024 the program has been scheduled 43 orbits. 2 targets suffered data loss so resulted in no usable observations (DESI-271.4849+70.9553 and DES0337-2958), while a third target (DESJ0145+0402) had incorrect sky coordinates so the target was not observed, resulting in 40 targets. See Table 1 for a summary and Figure 4 for the images.

The F606W filter was chosen to optimise flux from the typically $z_{\text{source}} > 1$ blue, star-forming source galaxies as well as from the rest-frame optical of the $z_{\text{deflector}} < 1$ massive quiescent deflectors. The input targets were selected from a series of lens candidate catalogues from the DES survey (Jacobs et al. 2019a,b; O'Donnell et al. 2022), DELVE survey (DECam Local Volume Exploration; Drlica-Wagner et al. 2021; Zaborowski et al.

¹ <https://sites.google.com/view/agelsurvey/science/hubble-images>

² STScI SNAP User Information Report

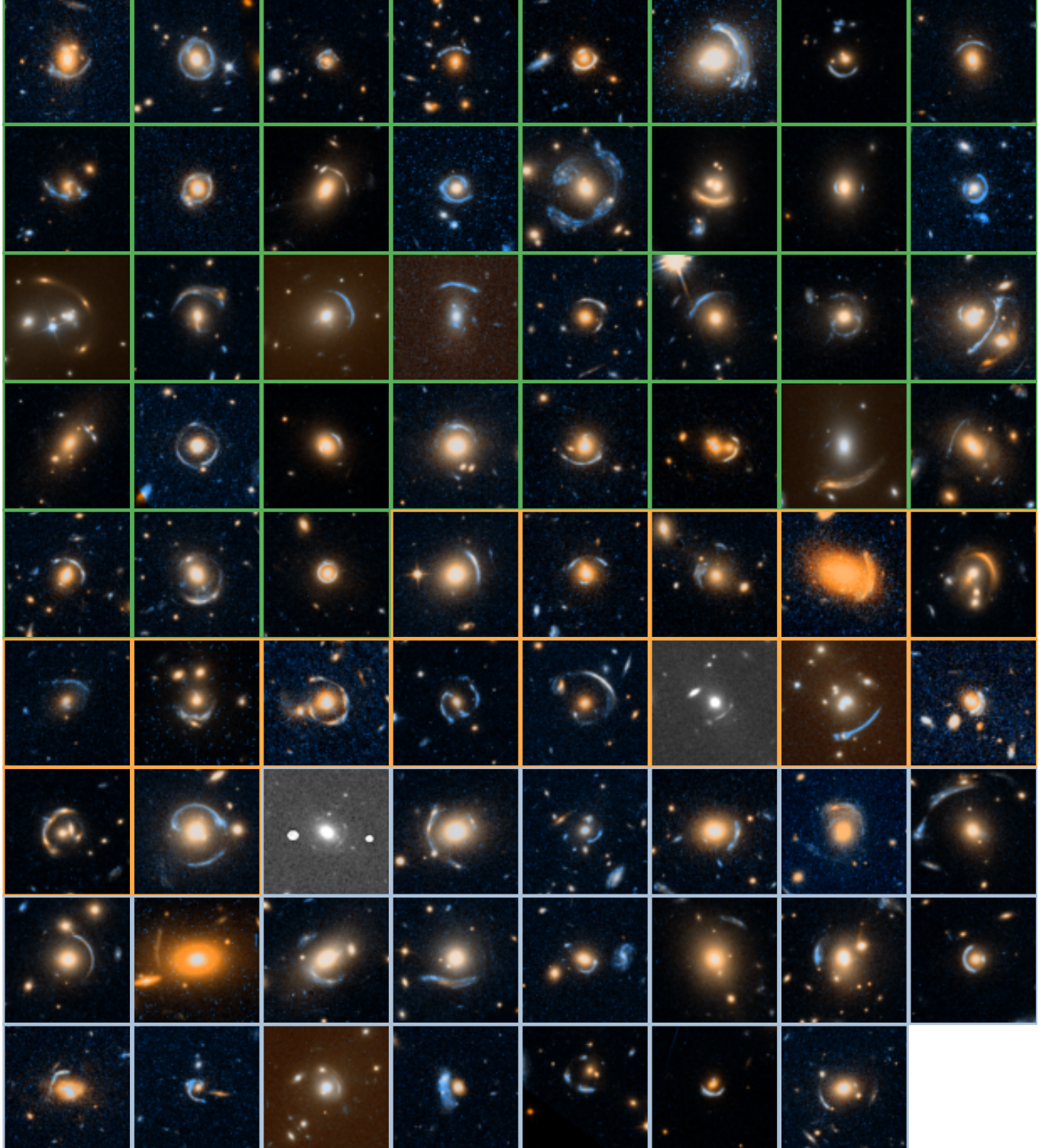


Figure 3. The 71 lenses imaged by HST SNAP program 16773 (PI Glazebrook). Targets bordered in green have confirmed deflector and source redshifts in the AGEL catalogue, targets bordered in orange have either a source or deflector redshift, while a grey border indicates no redshifts in AGEL. All images are $20'' \times 20''$ with north oriented up and east left. Object names are listed in Table A1.

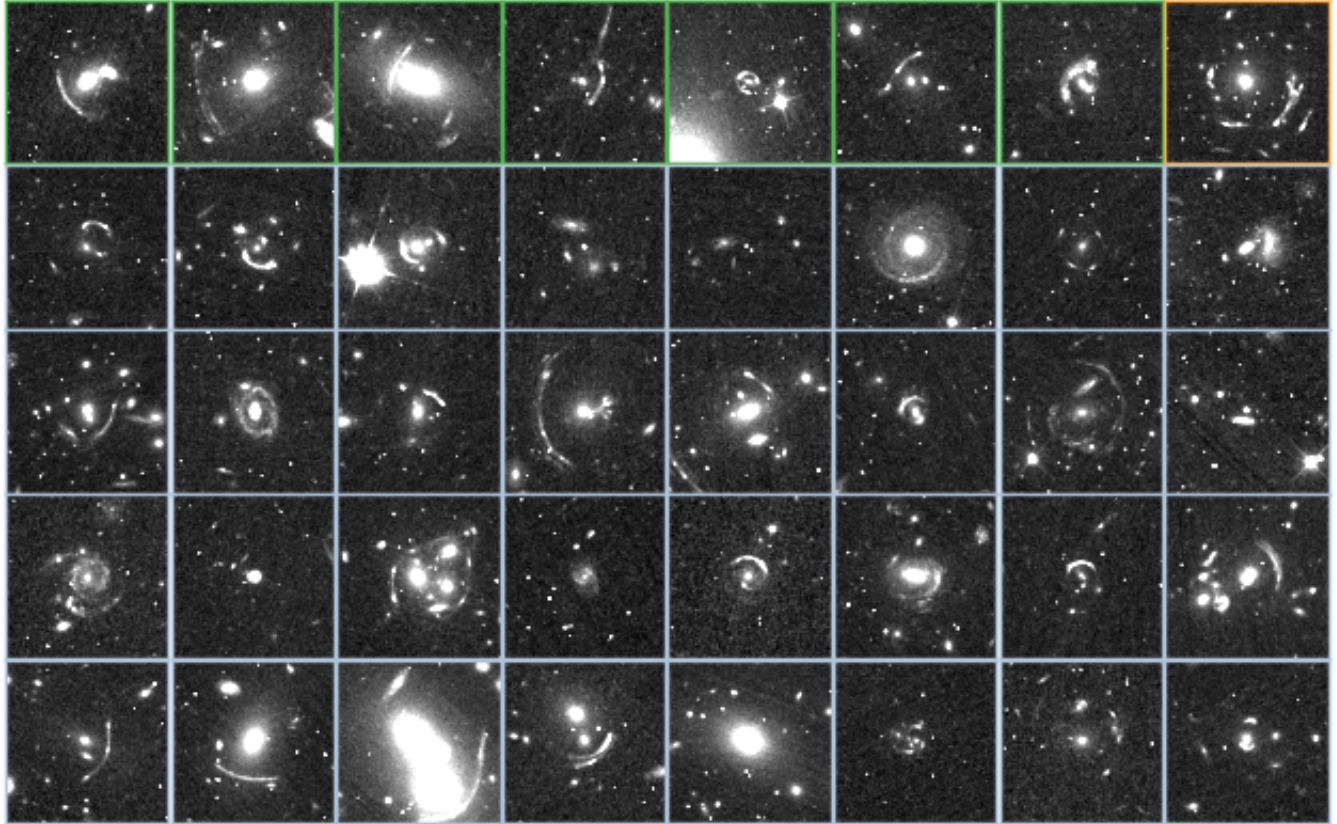


Figure 4. The 40 lenses imaged by HST GAP program 17307 (PI Tran). Targets bordered in green have confirmed deflector and source redshifts in the AGEL catalogue, targets bordered in orange have either a source or deflector redshift, while a grey border indicates no redshifts in AGEL. All images are $20'' \times 20''$ with north oriented up and east left. Object names are listed in Table A2.

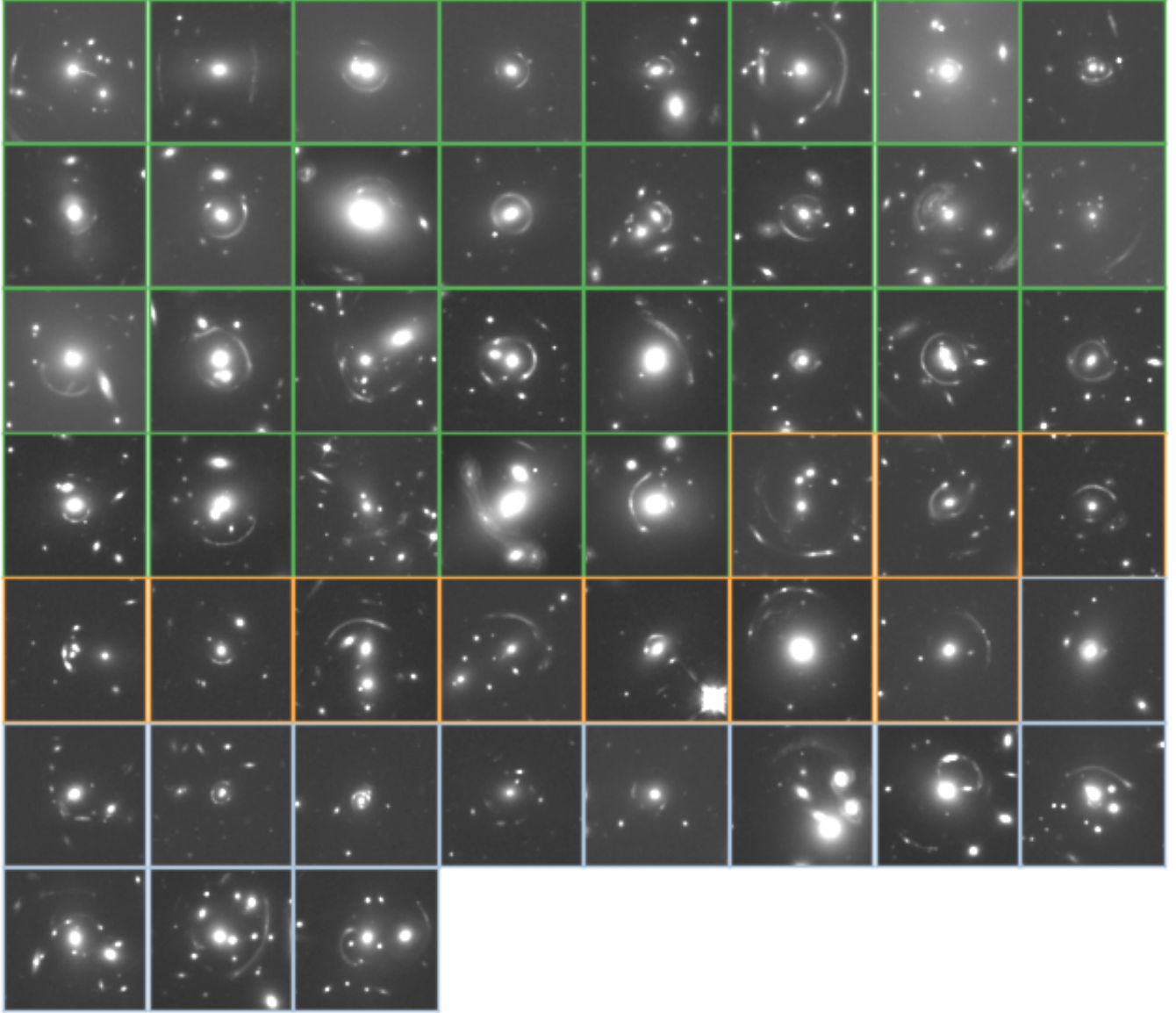


Figure 5. The 51 lenses imaged by HST SNAP program 15867 (PI Huang). Targets bordered in green have confirmed deflector and source redshifts in the AGEL catalogue, targets bordered in orange have either a source or deflector redshift, while a grey border indicates no redshifts in AGEL. All images are $20'' \times 20''$ with north oriented up and east left. Object names are listed in Table A3. See Huang et al. (2025) for further details of this program.

2023), HSC-SSP (Hyper Suprime-Cam Subaru Strategic Program; Sonnenfeld et al. 2020; Cañameras et al. 2021; Shu et al. 2022; Chan et al. 2024), DESI Legacy Imaging Survey (Huang et al. 2020, 2021; Storfer et al. 2022; Stein et al. 2022), and CASSOWARY survey (Stark et al. 2013).

2.3. WFC3 SNAP Program 15867, PI Huang

Many AGEL targets have also been observed by SNAP program 15867 (PI Huang; Huang et al. 2025) in cycle 27. This program obtained F140W imaging with

WFC3/IR for 51 targets³ with 20 minute exposures. See Table 1 for a summary, Figure 5 for the images and Huang et al. (2025) for further details.

3. SPECTROSCOPIC DATA

³ 53 targets were observed in total however 2 observations, DESI-158.2306+75.3149 and DESI-217.0936+03.3000, had failed guide star acquisitions resulting in full data loss. DESI-133.3800+23.3652 also had a failed guide star acquisition but still took useable data.

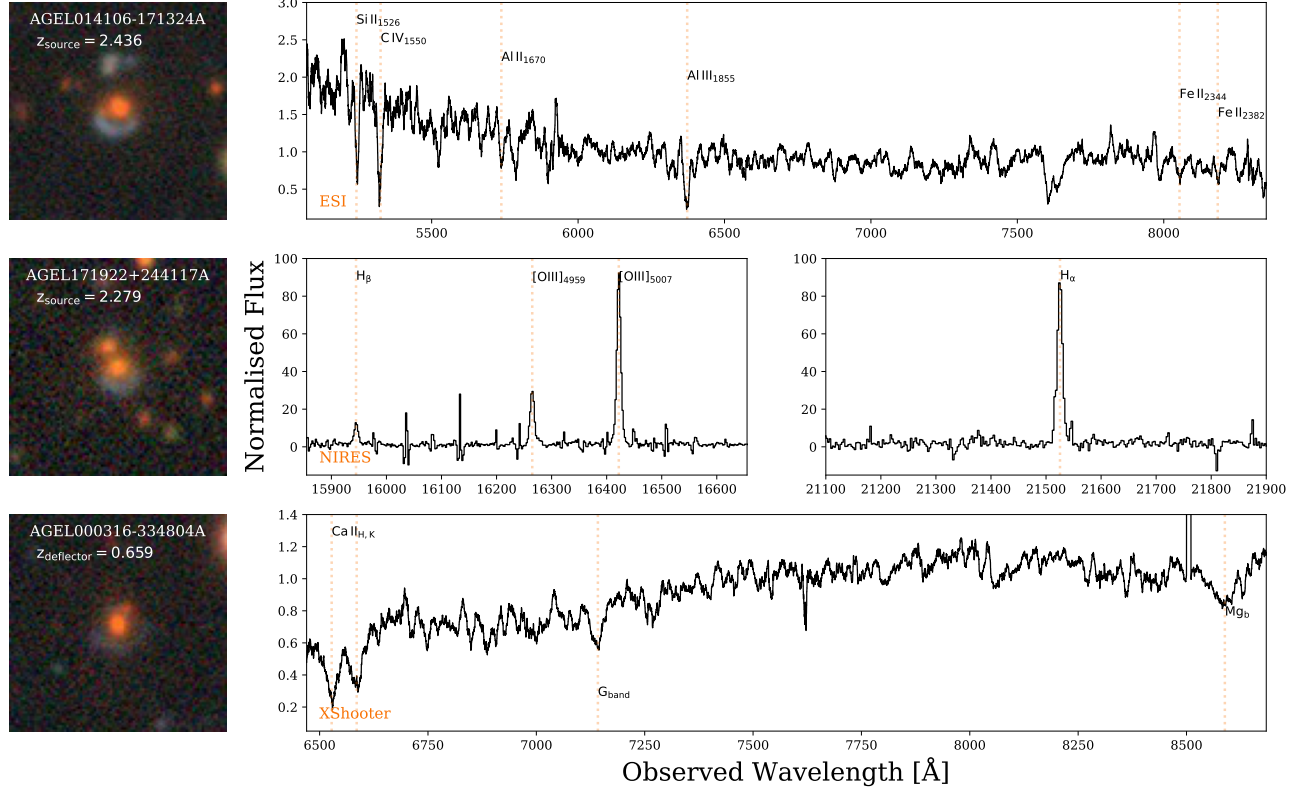


Figure 6. Example AGEL spectra. The top row shows the source spectrum from ESI with the $z = 2.436$ redshift measured from ISM absorption features. The middle row is a $z = 2.279$ NIREs source spectrum measured from nebula emission lines. The bottom panel is a $z = 0.659$ X-shooter deflector spectrum measured from stellar absorption features. grz $25'' \times 25''$ DECaLS images are shown in the left column with north oriented up and east left. Key spectral features used in the redshift measurement are shown with dotted orange lines. All spectra have a quality flag of 3.

AGEL spectroscopic targets were primarily drawn from Jacobs et al. (2019a,b), who used convolutional neural networks on the DES and DECaLS fields (Dey et al. 2019) to identify lens candidates. Additional targets were drawn from Huang et al. (2020, 2021) who similarly used a neural network approach on the DES and DECaLS fields. We note however that candidates from these catalogues may have been previously identified using other methods, e.g. some candidates had been previously identified by Diehl et al. (2017) using a colour and magnitude selection in the DES catalogues. Therefore, while we include in Table 4 the origin of each system, this may not be the systems's first reported discovery and simply reflects the catalogue we obtained the candidate from.

3.1. Measuring Redshifts

To measure the redshifts we used different spectral features depending upon the target's redshift, the observed wavelength coverage and the relative strength of the spectral features. The deflectors are generally massive passive galaxies (or small groups of quiescent galaxies) at $z \sim 0.5$, and therefore redshift confirmation

is most easily achieved via the rest-frame optical stellar absorption features CaII_{H,K}, Balmer series absorption, Mg_b, and Nad. We therefore required sufficient continuum S/N over a wide wavelength range to detect these absorption features. To this end, we primarily used Keck/ESI and VLT/X-shooter to obtain deflector redshifts. On the other hand the lensed sources tend to be $z > 1$ star-forming galaxies with bright rest-frame optical emission lines⁴. This motivated the choice of Keck/NIREs and VLT/Xshooter for source redshifts, which cover rest-frame optical emission lines for $z > 1$ sources. This approach also allowed us to measure strong interstellar absorption and stellar wind features such as SiIII, CIV, FeII, and MgII for many of the sources (e.g. Keerthi Vasan et al. 2023). See Figures 6 and 7 for example spectra. In addition to the primary spectroscopic observing programs using X-shooter, ESI and NIREs, additional redshifts were measured using

⁴ We confirmed two sources that are $z > 1$ quiescent galaxies (Zhuang et al. 2023), with most red sources being dusty star-forming systems.

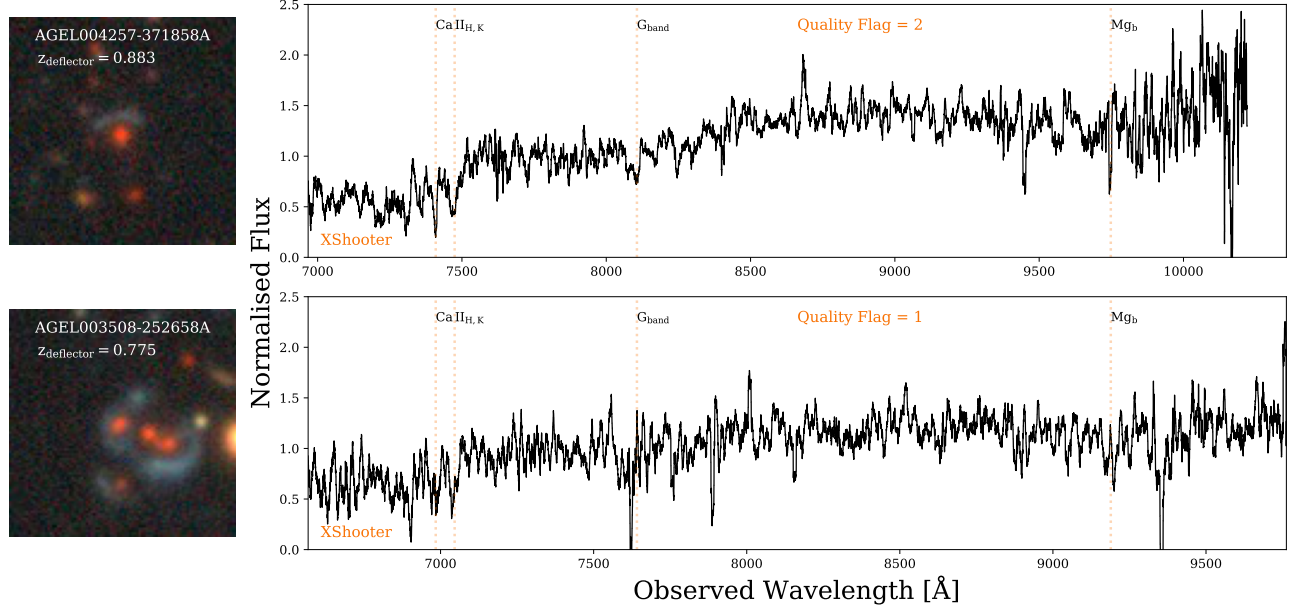


Figure 7. Example AGEL spectra of varying redshift quality flags. The top row is a deflector spectrum from X-shooter with redshift quality flag= 2, and the bottom row is a deflector spectrum from X-shooter with quality flag= 1. $grz 25'' \times 25''$ DECaLS images are shown in the left column with north oriented up and east left. Key spectral features used in the redshift measurement are shown with dotted orange lines.

Keck/MOSFIRE, Keck/KCWI, and KECK/DEIMOS. We detail the observing strategies and data reduction pipelines used with each instrument in the following subsections.

Tables 4 and 5 summarise all the measured redshifts. Each redshift includes a (subjective) quality flag indicating the reliability of the measurement (3 = high, 1 = low). A redshift flag of 3 indicates a reliable measurement from multiple well-detected features; see Figure 6 for example spectra with quality flags = 3. A flag of 2 indicates one strong line and a possible weak second line or second line obscured by telluric features, or multiple features in a low S/N spectrum. A flag of 1 was given if only a single feature was observed, or the S/N was low enough to make the redshift measurement uncertain. See Figure 7 for example spectra with quality flags of 1 and 2. To refine the redshifts we used a mixture of fitting Gaussians to emission and absorption features as well as the online redshifting software MARZ (Hinton et al. 2016) to fit templates to multiple features.

The redshifts all have formal uncertainties of ± 0.0005 , with the following caveats: (a) redshifts with a lower quality flag are less certain (flag 2 will have lower precision, flag 1 lower accuracy and/or precision); (b) redshifts measured from ISM features are likely to be slightly blueshifted from the systemic velocity due to outflows (e.g. Keerthi Vasan et al. 2023); and (c) depending upon the inclination and lensing geometry the measured red-

shift may also be convolved with internal galaxy rotation.

3.2. Keck/NIRES and ESI

The primary instruments used for northern and equatorial targets were Keck’s ESI (Echellette Spectrograph and Imager; Sheinis et al. 2002) and NIRES (Near-Infrared Echellette Spectrometer; Wilson et al. 2004), with ESI used primarily to obtain deflector redshifts and NIRES to measure high ($z > 1$) redshift sources.

67 redshifts were measured with NIRES using total exposure times of typically 20 minutes (using an ABBA dither pattern). NIRES has a fixed slit of $0.55'' \times 18''$ providing a mean spectral resolution of $R = 2700$ over the wavelength range $0.9 - 2.45\mu\text{m}$ with a pixel scale of $0.15''/\text{pixel}$. We reduced the data using the NSX pipeline developed by T.Barlow⁵ and used the 2D echelle-corrected data produced by the pipeline to extract the 1D spectra.

We obtained 51 redshifts using ESI in its echelle mode with the $1.0'' \times 20''$ slit, providing wavelength coverage of $3900 - 10900 \text{ \AA}$ at a resolving power of $R = 4000$. Exposure times varied depending upon the brightness of the target and weather conditions, with typical total exposures between 20 – 80 minutes. Early observations (programs 2019B_W226, 2019_U058) were reduced using

⁵ <https://sites.astro.caltech.edu/tb/nsx/>

AGEL Name (1)	HST object name (2)	Comment (3)
AGEL211515+101153A	DCLS2115+1011	Ring galaxy
AGEL215041+140248A	DECALS 6508900	Ring galaxy
AGEL224400+124540A	DCLS2244+1245	Red star + blue galaxy
AGEL203459+001636A	DECALS 1727734	Red star + blue galaxy
AGEL131330-064211A	DCLS1313-0642	Red Galaxy + blue blob (not spectroscopically confirmed)
AGEL132557+263659A	DCLS1325+2636	Red Galaxy + blue blob (not spectroscopically confirmed)

Table 2. False-positive targets. (1) AGEL object name, (2) object name used in the HST observations, (3) target details.

the ESIREDUX software provided by J. X. Prochaska⁶. Later observations (2020 onwards) were reduced using MAKEE written by T. Barlow⁷.

3.3. VLT/X-shooter

We use the X-shooter instrument (Vernet et al. 2011) on the Very Large Telescope to obtain 62 redshifts. X-shooter provides slit spectral coverage over the wavelength range $3000 - 25000 \text{ \AA}$. The data was obtained in programs 0101.A-0577 (PI Glazebrook), 105.20KF.001 (PI Lopez), and 108.22JL.001 (PI Lopez). In program 0101.A-0577 exposure times ranged between 10-40 minutes for deflectors and 40-60 minutes for the sources, with the source and deflector occasionally targeted in the same exposure. For programs 105.20KF.001 and 108.22JL.001, source and deflector spectra were taken separately with typically 30 minute exposures for the deflectors and 60 minute exposures for the sources. We used slit widths of $1.0''$ ($R=5100$), $0.9''$ ($R=8800$) and $0.9''$ ($R=5600$), for the UVB ($3000 - 5600 \text{ \AA}$), VIS ($5600 - 10240 \text{ \AA}$) and NIR ($10240 - 24800 \text{ \AA}$) arms respectively.

The data was reduced using the ESO REFLEX pipeline (Modigliani et al. 2010) to obtain 2D flux calibrated spectra in air wavelengths. The flux calibration was performed using standard stars taken during the respective observing night. We then extracted 1D spectra using the SPECLIB software package written by C. Schreiber⁸.

3.4. Keck/KCWI

We used the Keck cosmic Web Imager (Morrissey et al. 2018) to obtain 14 spectra. We used the medium slicer with the blue low resolution (BL) grating, which provides a resolution of 2.5 \AA FWHM ($R \approx 1800$) in the wavelength range $3500 - 5600 \text{ \AA}$ in a $16.5'' \times 20.4''$ field of view. We reduced the data using the IDL and Python

versions of the KCWI data reduction pipeline⁹ using the standard steps. For complete details of the data reduction process see Keerthi Vasan G. et al. (2024).

3.5. Keck/MOSFIRE

9 targets were observed using Keck’s MOSFIRE instrument (Multi-Object Spectrometer For Infra-Red Exploration; McLean et al. 2012) as filler targets for program 2022A_W223 (PI Nanayakkara). The observations on AGEL targets used the $1.0'' \times 60''$ longslit in the H-band ($R=3600$ over $1.47 - 1.80 \mu\text{m}$) with additional exposures in the K-band ($R=3610$ over $2.03 - 2.40 \mu\text{m}$) if needed. The data was reduced using the publicly available pipeline¹⁰ using the procedure outlined in Nanayakkara et al. (2016). For more information about the observing run, see Antwi-Danso et al. (2023).

3.6. Keck/DEIMOS

We targeted 1 system, AGEL235934+020824A, with the Keck/DEIMOS instrument (2022B_U099, PI Jeltema). We used two different instrument configurations. The first configuration targeted the central galaxy as well as candidate cluster galaxies in the field with the 1200G grating, yielding a spectral range of roughly $5200 - 8000 \text{ \AA}$. The second configuration targeted the lensed source as well as candidate cluster galaxies, using the 600ZD grating for maximum wavelength coverage. All data from this night were reduced with PypeIt version 1.11.0 (Prochaska et al. 2020; Prochaska et al. 2020). While the spectrum of the deflector galaxy yielded a highly confident redshift, the source spectrum detected no features. The lensed source was later targeted by NIRES (2023B_U039, PI Jeltema), obtaining a confident redshift.

4. SAMPLE CHARACTERISTICS

4.1. Impostors

⁶ <https://www2.keck.hawaii.edu/inst/esi/ESIRedux/>

⁷ <https://sites.astro.caltech.edu/tb/makee/>

⁸ <https://github.com/cschreib/speclib>

⁹ <https://kcwi-drp.readthedocs.io/en/latest/>

¹⁰ <http://keck-datalreductionpipelines.github.io/MosfireDRP/>

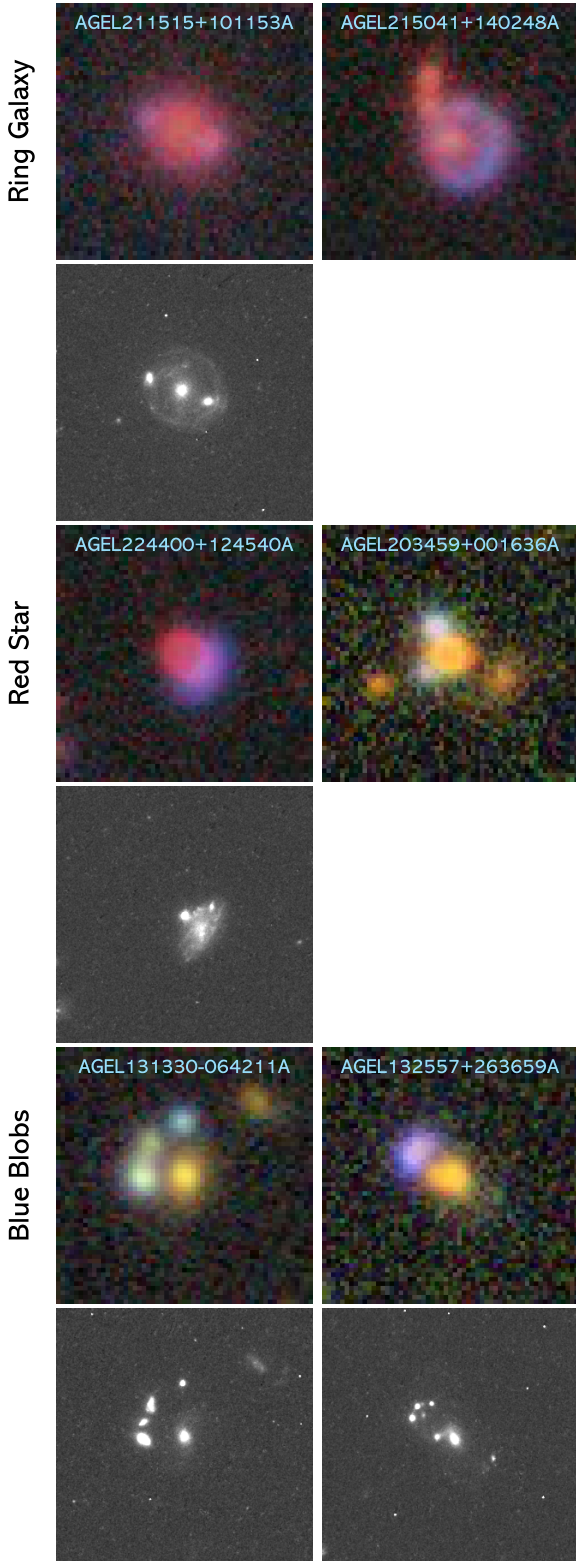


Figure 8. The 6 candidates found to not be lenses, showing the DECaLS grz on the top and the F200LP HST image (if available) beneath it. The 6 false-positives fall into 3 categories: ring galaxies, red stars, and blue blobs. All images are $15 \times 15''$ and are oriented with north up and east left.

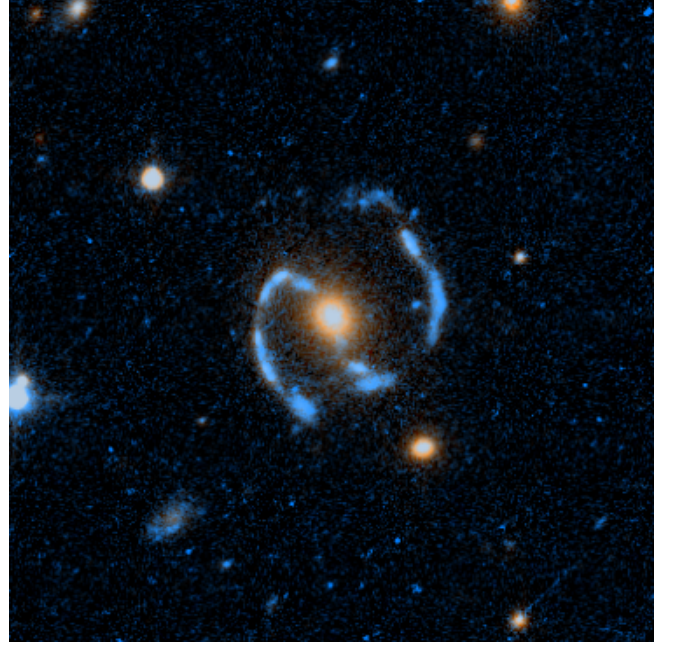


Figure 9. AGEL085413-042409A has a morphology reminiscent of a barred spiral, but is comprised of two $z = 2.393$ galaxies multiply lensed by a $z = 0.856$ galaxy deflector. The image is $20'' \times 20''$ with north oriented up and east left.

The AGEL lens confirmation campaign has achieved a high success rate (96 %), however during the course of the survey we have identified 6 lens candidates which, upon spectroscopic and/or photometric followup, were identified as false-positives. Identifying the common causes of impostors is important to ensuring high fidelity samples in upcoming large area surveys such as LSST and Euclid. We therefore present these false positives in Figure 8, and briefly discuss their morphologies.

The 6 false-positives fall into 3 categories: (a) ring galaxies, (b) a red star in front of blue galaxies, and (c) red galaxies next to irregular blue blobs (see Table 2). The first category, ring galaxies, need spectroscopic redshifts to identify as shown by the still-convincing HST imaging for AGEL211515+101153 in Figure 8. The second category, red stars, could be reduced by cross-matching candidate lists with large catalogues of stars. For example, SDSS uses SED fitting to multi-band photometry to classify targets as stars, galaxies or quasars. However this approach would not completely eliminate red stars as in the example of AGEL224400+124540A which is classified as a galaxy in SDSS, likely due to the light from the blue galaxy behind it contaminating the photometry. Finally, red galaxies next to irregular blue blobs are difficult to eliminate without higher resolution imaging. However upon close inspection the 3 blobs of AGEL131330-064211A have slightly different colours in the DECaLS grz imaging leaving it unlikely it is the

same object multiply lensed. To rule out false positives, next generation neural network lens finders should aim to take advantage of multiband photometry to (i) accurately identify galaxy deflectors from red stars, and (ii) find candidate arcs with identical colours. High resolution multi-band images from Euclid should therefore significantly improve future high-fidelity lens searches.

While high resolution imaging can usually confirm the lensing nature of candidates, it is not always sufficient and occasionally spectra is also required. AGEL085413-042409A (Figure 9) has a morphology reminiscent of spiral arms, and as a result HST imaging alone did not definitively confirm whether AGEL085413-042409A is a lens or whether the blue arcs are barred spiral arms or features of a merger. Integral field spectroscopy with Keck/KCWI confirmed the blue “arms” are two $z = 2.393$ galaxies, both multiply lensed by a $z = 0.856$ galaxy deflector.

4.2. Comparison to other surveys

We explore how the AGEL sample compares in redshift distribution from previous lens samples. Following Tran et al. 2022, in the following comparisons we include all targets which satisfy the following criterion: spectroscopic redshifts for the foreground deflector and/or background source which have a quality flag ≥ 2 (see Section 3.1 and Figures 6 and 7 for definitions of the quality flag). This criterion removes 12 targets.

As discussed previously in Tran et al. 2022, candidate lenses were prioritised for spectroscopic observations if (a) they were at suitable RA and DEC for the allocated observations, (b) they had high resolution imaging, and (c) they appeared to be lenses in visual inspection of available imaging. It is therefore difficult to directly compare the resulting AGEL sample to surveys such as SLACS, BELLS, and CSWA and SL2S with comparatively well defined selection functions. As shown by Figure 10, the deflector r-band magnitudes of the spectroscopic sample differ slightly to the parent candidate samples of Jacobs et al. (2019a,b) and Huang et al. (2020, 2021). Comparing the DR2 sample to 1000 random realisations of the parent sample, we find the DR2 sample is slightly broader than parent distribution (although the standard deviations are consistent within 2σ) and with means consistent within 1σ . This excess in the spectroscopic sample to fainter deflector magnitudes likely reflects the $z > 0.5$ science cases in mind for AGEL deflectors (e.g. Sahu et al. 2024; Barone et al. 2024). However, for the purposes of the following comparison, we consider the AGEL sample as representative of the total candidates found by neural networks. In the following section we consider how differences in the

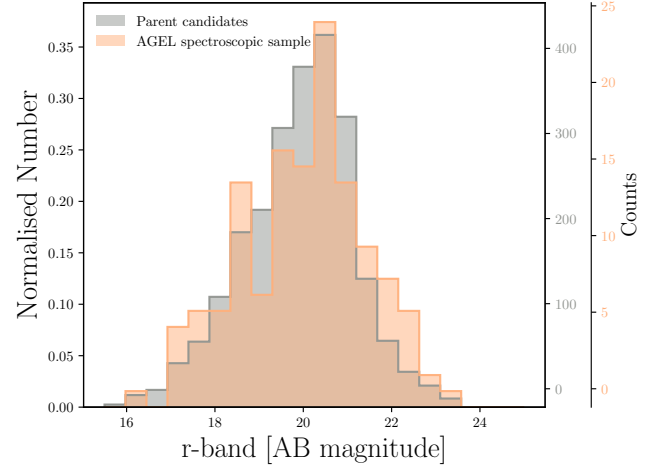


Figure 10. Number density histogram of deflector r-band magnitudes. The AGEL parent candidate sample from Jacobs et al. (2019a,b); Huang et al. (2020, 2021) is shown in grey, with the spectroscopic sample in orange. Based on 1000 realisations of the parent sample, we find the two distributions statistically consistent.

AGEL sample to literature samples may be reflective of differences in identification methods.

Figure 11 shows the deflector and source redshift distributions for the AGEL sample (candidates identified in DES and DECaLS imaging via neural networks), SLACS and BELLS (identified in SDSS single-fibre spectroscopy), CASSOWARY (identified via blue sources close to luminous red galaxies in SDSS imaging), and SL2S (blue sources close to luminous red galaxies in CFHT imaging). The different selection methods evidently lead to different deflector and source distributions.

Firstly, the redshift distributions of the fibre based search surveys are intrinsically linked to the aperture of the fibre ($3''$ diameter for SLACS and $2''$ diameter for BELLS). The Einstein radius θ_E of a single isothermal sphere is:

$$\theta_E = 4\pi \frac{\sigma_v^2}{c^2} \frac{D_{ds}}{D_s} \quad (1)$$

For D_{ds} the angular diameter distance between deflector and source, D_s the distance between observer and source, and σ_v the velocity dispersion of the deflector. Therefore, for fixed deflector velocity dispersion, $\theta_E \propto \frac{D_{ds}}{D_s}$. We can see this in Figure 11c where the source redshifts tend to be more correlated to the deflector redshifts in the SLACS and BELLS samples (Spearman coefficients of $\rho = 0.44$ and 0.70 respectively) than the image-based search samples (c.f. $\rho = 0.38$, 0.45 and 0.24 for AGEL, CASSOWARY and SL2S).

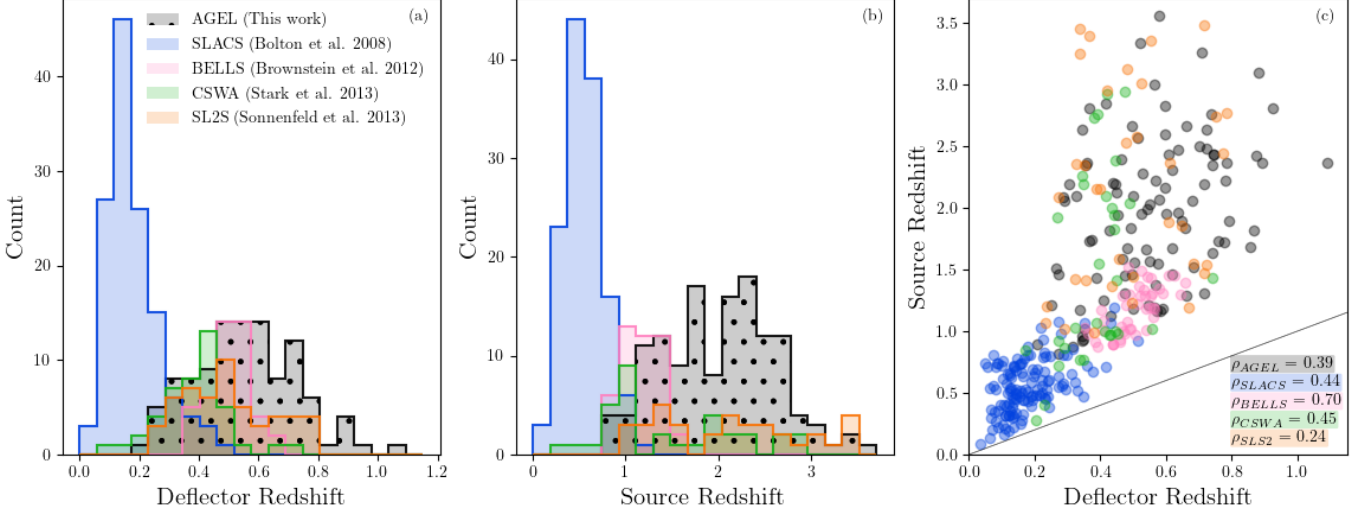


Figure 11. Comparison of the AGEL spectroscopic sample to other lensing samples. Panel (a) shows the deflector redshifts, (b) the source redshifts (all redshifts spectroscopically confirmed). The AGEL sample spans to higher source and deflector redshifts than most previous samples. Panel (c) shows the relationship between source and deflector redshifts, with the Spearman rank-order correlation coefficient for each sample annotated in the bottom right corner. All the samples have $p\text{-value} << 0.05$ except for SL2S, implying that SL2S is the only sample in which the source redshift is independent to the deflector redshift. The grey line in panel (c) shows the one-to-one relation.

By virtue of the deeper sensitivities of DES and DECaLS imaging ($r_{DES, DECaLS} = 23.4$ compared to $r_{SDSS} = 22.70$) our sample spans higher redshifts for both deflectors and sources than the SDSS based surveys (SLACS, BELLs, CSWA).

The SL2S and AGEL deflector distributions are most similar. CFHTS has slightly deeper imaging than DECaLS ($r_{CFHTS} = 24.5$), however DECaLS covers a significantly larger area ($\sim 9000 \text{ deg}^2$ compared to CFHTS $\sim 170 \text{ deg}^2$). Noticably, although AGEL has more $z_{\text{deflector}} > 0.8$ (possibly due to the larger search area), the SL2S source redshifts skew higher, likely due to the deeper imaging. Similarly to AGEL, SL2S used a range of telescopes and instruments for spectroscopic follow-up. Therefore whether a redshift was securely measured (both in AGEL and SL2S) depends upon the wavelength coverage and sensitivity of the various instruments.

The number density of galaxy-scale lenses detected in wide-area surveys is sensitive to cosmology. From the AGEL redshift sample we select a subset of 36 that have (i) both source and deflector redshifts, and (ii) have a single-galaxy deflector based on the DECaLS grz imaging. We compare the redshift distribution of this galaxy-scale subset to the distribution predicted by the analytical model GALESS¹¹ (Ferrami & Wyithe 2024), assuming the limiting magnitudes of the DECaLS imaging ($g = 24.0$, $r = 23.4$ and $z = 22.5$). For the model

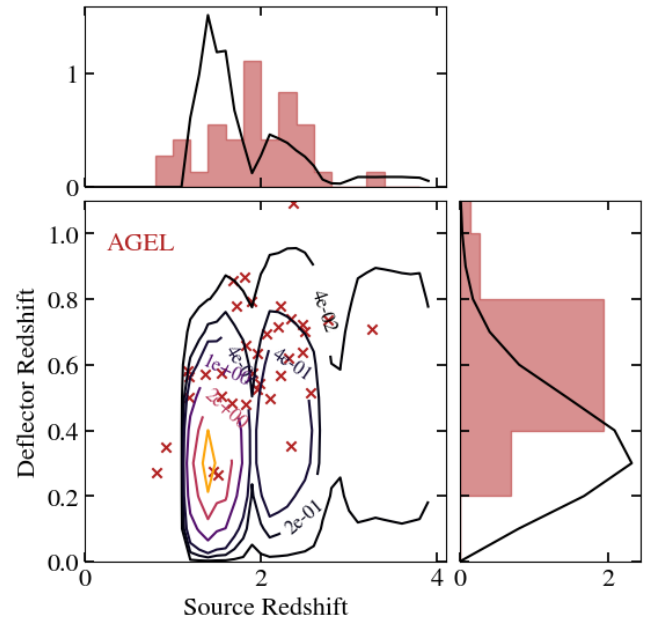


Figure 12. Comparison between the redshift distribution of the AGEL galaxy-scale subsample (red crosses and histograms) and predictions from the GALESS analytical model (contours and black solid line; Ferrami & Wyithe 2024). AGEL systems skew to higher redshift deflectors than expected by the model.

we limit the source redshifts to the intervals in which at least two emission lines out of H_α , H_β , $[O_{III}]$, and $[O_{II}]$ can be detected in NIR infrared spectroscopy. The resulting number density distribution is shown in Figure

¹¹ <https://github.com/Ferr013/GALESS/>

AGEL Name (1)	HST object name (2)	HST program ID (3)	z_A (4)	z_B (5)	z_{DE} (6)
AGEL150745+052256	DCLS1507+0522	16773	2.163	2.591	0.594
AGEL080820+103142	DESI-122.0852+10.5284	15867	1.303	1.452	0.475
AGEL035346-170639	DCLS0353-1706	16773	1.674	1.46	0.617
AGEL013442+043350	DESI-023.6765+04.5639	15867	1.568	2.03	0.55
AGEL144149+144121	DESI-220.4549+14.6891	15867	1.433	2.34	0.741
AGEL024303-000600	DESJ0243-0006	16773	1.729	0.506	0.367

Table 3. Galaxy-scale double source lenses. The columns are as follows: (1) The object label used in the AGEL catalogue. (2) Object name used in the HST observations. (3) ID of the observing program the HST images came from; ID:16773 (PI Glazebrook) has filters F140W and F200LP and ID:15867 (PI Huang) has just the F140W filter. (4) and (5) show the redshifts of the arcs as labelled in Figure 13. (6) Deflector redshift.

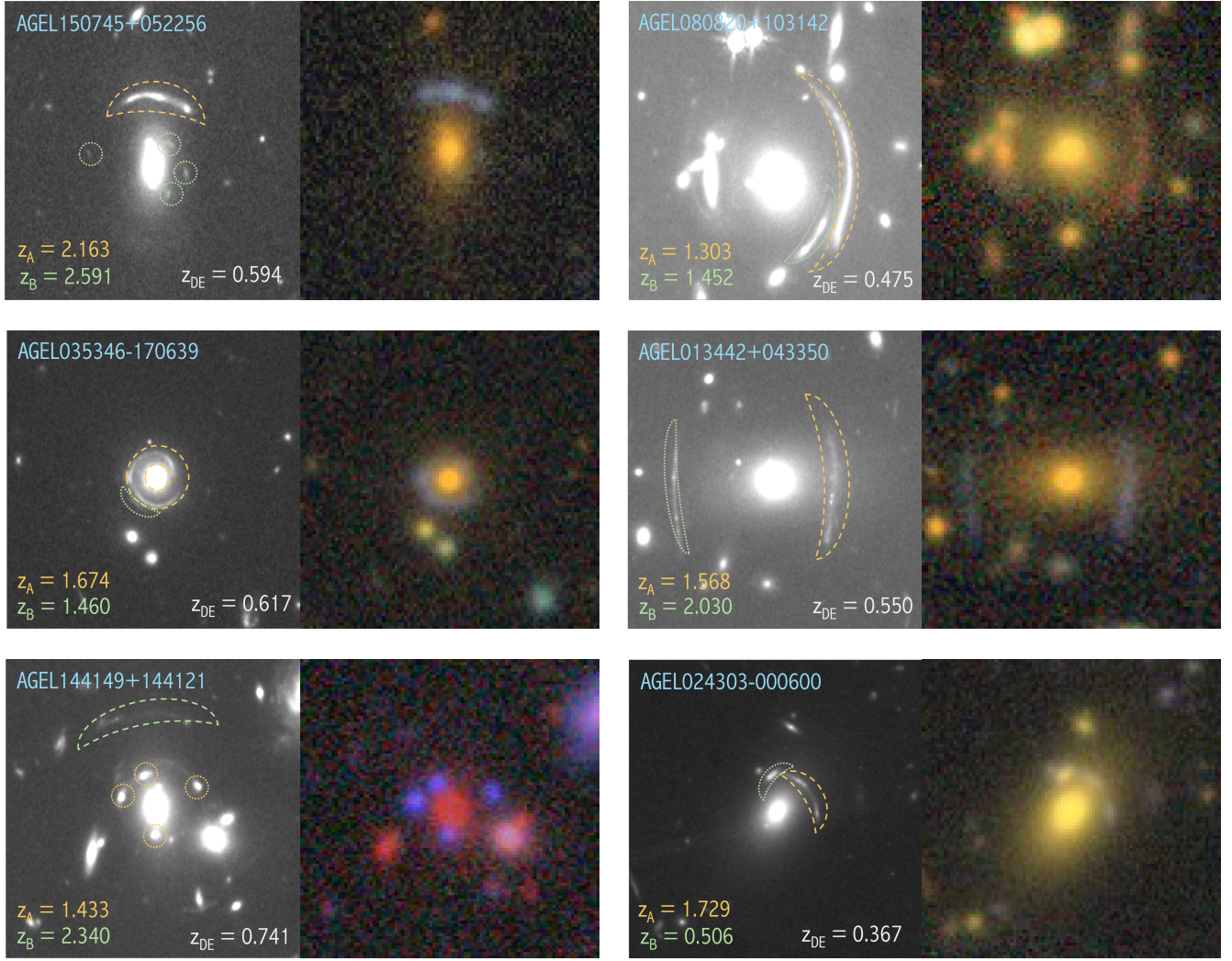


Figure 13. Galaxy-scale multi-source lenses, with the HST/F140W image in the left column and DECaLS *grz* in the right column. Arc A is highlighted by the orange dashed shapes and arc B by the green dotted shapes. The redshifts are labelled in the HST panels. All images are $25 \times 25''$ and are oriented with north up and east left.

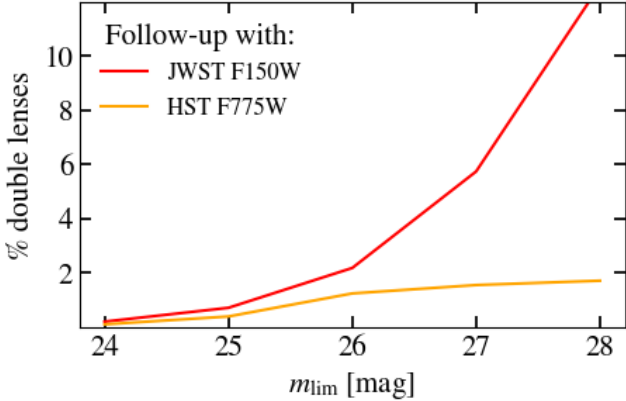


Figure 14. Prediction on the fraction of galaxy-scale lenses originally identified in DECaLS photometry that are expected to show additional lensed arcs if observed in F150W (red line) and F775W (orange line) filter observations, based upon the limiting magnitude (m_{lim}) of those observations. Prediction based on semi-analytical model GALESS (Ferrami & Wyithe 2024)

12. From Figure 12, AGEL deflectors skew to higher redshifts ($z \sim 0.6$) than predicted by the model (which peaks at $z \sim 0.3$). This may be related to the subtle skew in AGEL deflectors to fainter r-band magnitudes than the parent catalogue (Figure 10), potentially reflecting the team’s science preference towards identifying higher redshift deflectors.

4.3. Double Source Plane Lenses

A key science case driving the need for large lens samples with high-resolution imaging is cosmology via double source plane galaxy-scale lenses (gravitational lens cosmography; Blandford & Narayan 1992; Treu 2010).

The ideal system for gravitational lens cosmography is one that has (i) a deflector with a simple mass distribution, and (ii) numerous, multiply lensed arcs at a large range of redshifts. Galaxy-scale lenses satisfy the first criterion, with mass profiles that are close to single isothermal spheres. However, galaxy-scale systems rarely lens more than one source (the current record is 3; Collett & Smith 2020), so seldom satisfy the second criterion. In theory, gravitational lens cosmography is possible from single source systems (e.g. Biesiada et al. 2010), but the cosmological parameters are highly degenerate with the choice of the deflector mass density profile. A second multiply lensed source provides additional constraints on the mass distribution and therefore reduces this degeneracy (Collett & Auger 2014; Smith & Collett 2021). Furthermore the constraining power of each system depends upon the relative redshifts of the sources, with a low separation lens-source combined

with a second high redshift source proving ideal (Collett et al. 2012). Therefore, searching for and building a sample of multi-source galaxy-scale is valuable, as even just ~ 10 systems would provide cosmological constraints with a precision comparable (and orthogonal) to all current supernovae and galaxy surveys (Collett et al. 2012).

We present 6 double source plane lenses in the AGEL survey (Table 3 and Figure 13). These targets were identified by visual inspection of HST imaging and redshifts confirmed spectroscopically. The importance of high resolution imaging to (a) identify faint secondary arcs and (b) identify any possible satellite or neighbouring galaxies is illustrated in Figure 13.

The probability of a galaxy acting as a gravitational lens scales with the velocity dispersion (σ) of the galaxy: $P(\text{lens}) \sim \theta_E^2 \sim \sigma^4$ where θ_E is the lensing cross section. Hence a sample of galaxy-scale lenses is biased to be more massive than randomly drawn galaxies. Consequently, the conditional probability of observing a second lensed image behind a galaxy-scale lens is higher than the probability of finding a single lens in the first place. Furthermore, AGEL targets were selected from ground-based surveys so the seeing limit in the images leads to only identifying lenses with large Einstein radii. Therefore, just the higher spatial resolution of space telescope images increases the chances of identifying additional arcs with smaller Einstein radii. Combined with the typically deeper sensitivities of space telescope images results in a significantly higher probability of identifying secondary arcs given a first.

To quantify the conditional probability of finding additional arcs, we use the analytic model described in Gavazzi et al. (2008) and implemented in GALESS (Ferrami & Wyithe 2024) to predict the fraction of AGEL galaxy-scale lenses we expect to have additional arcs detectable in HST WFC3/F775W and JWST NIRCam/F150W imaging (Figure 14). At limiting magnitudes fainter than 26 we see a significant increase in the fraction of double-source plane lenses detected in the redder F150W filter, as the redder filter is sensitive to higher redshift arcs. Future JWST observations with redder bands therefore have the potential to significantly increase the sample of known double-source plane lenses. In HST programs 16773 and 15867 (with F140W AB limiting magnitudes of approximately 26), we count a total 6 double-source galaxy-scale lenses out of 125 (5 %), slightly higher but similar to the 2 % predicted by the model for the similar F150W filter. However, the local environment of these lenses is not well constrained—these targets were identified as “galaxy-scale” by visual inspection of the available imaging. While the arcs ap-

pear deflected by a single galaxy, that single galaxy may itself be part of a larger group.

Parts of this research were conducted by the Australian Research Council Centre of Excellence for All Sky Astrophysics in 3 Dimensions (ASTRO 3D), through project number CE170100013. T.M.B, K.G, D.J.B, and G.F.L acknowledge support from Australian Research Council Discovery Project grant DP230101775. TJ, KVGC, and FD gratefully acknowledge support from the National Science Foundation through grant AST-2108515, the Gordon and Betty Moore Foundation through Grant GBMF8549, and a UC Davis Chancellor’s Fellowship. X.H. acknowledges the University of San Francisco Faculty Development Fund. Support for HST program 15867 was provided by NASA through a grant from the Space Telescope Science Institute, which is operated by the Association of Universities for Research in Astronomy, Inc., under NASA contract NAS 5-26555. S.L. and N.T. acknowledge support by FONDECYT grant 1231187. S.M.S acknowledges funding from the Australian Research Council (DE220100003). Some of the data presented herein were obtained at the W. M. Keck Observatory, which is operated as a scientific partnership among the California Institute of Technology, the University of California and the National Aeronautics and Space Administration. The Observatory was made possible by the generous financial support of the W. M. Keck Foundation. The authors wish to recognize and acknowledge the very significant cultural role and reverence that the summit of Maunakea has always had within the indigenous Hawaiian community. We are most fortunate to have the opportunity to conduct observations from this mountain.

5. SUMMARY

The AGEL survey is an ongoing effort to create a large sample of spectroscopically confirmed gravitational lenses with high-resolution imaging. Thus far we have obtained high-resolution HST imaging of 111 targets, as well as 204 redshifts associated with 138 lens systems. Compared to previous samples, AGEL lenses span higher source and deflector redshifts.

Due to the flexible neural network search algorithm, there is a large diversity of targets within AGEL. Deflectors range from individual galaxies all the way up to clusters, and sources span from highly star-forming to long quiescent. As a result, AGEL targets benefit a large range of science topics, including the baryon cycle (Keerthi Vasan et al. 2023; Barone et al. 2024), the build-up of chemical elements (Zhuang et al. 2023), and mass assembly (Sahu et al. 2024; Sheu et al. 2024). The insights learnt from the AGEL sample will help to refine lens searches on future large-area surveys.

Facilities: HST(WFC3), HST(ACS), Keck(NIRES), Keck(ESI), Keck(LRIS), Keck(KCWI), Keck(DEIMOS), Keck(MOSFIRE), VLT(X-shooter)

Software: Astropy, NumPy, Matplotlib, Montage, Pandas, reproject.

Object Name (1)	z _{source} (2)	Source flag (3)	Source Proposal ID (4)	z _{deflector} (5)	Deflector flag (6)	Deflector Proposal ID (7)	HST Imaging (8)		Candidate Catalogue (9)		RA (10)	Dec (11)
AGEL000224-350716A	1.549	3.0	LOPEZ_105.20KF.001_XShooter	0.576	3.0	LOPEZ_105.20KF.001_XShooter			Jacobs et al. 2019a,b	0.59845	-35.12122	
AGEL000316-334804A	1.834	3.0	LOPEZ_105.20KF.001_XShooter	0.659	3.0	LOPEZ_105.20KF.001_XShooter			Jacobs et al. 2019a,b	0.81825	-33.80120	
AGEL000645-442950A	2.099	3.0	LOPEZ_105.20KF.001_XShooter	0.498	3.0	LOPEZ_105.20KF.001_XShooter			Jacobs et al. 2019a,b	1.68592	-44.49735	
AGEL000729-443446A	1.009	3.0	LOPEZ_108.223L.001_XShooter						Jacobs et al. 2019a,b	1.87201	-44.57949	
AGEL001310_-004004A	2.071	1.0	JONES_2019A_U058_ESI	0.693	3.0	JONES_2019B_U058_ESI			Jacobs et al. 2019a,b	3.29016	0.66767	
AGEL001424_-004145A	1.374	3.0	GLAZEBROOK_0101.A-0577_XShooter	0.569	3.0	GLAZEBROOK_0101.A-0577_XShooter			Jacobs et al. 2019a,b	3.60116	0.69596	
AGEL001702-100911A	1.831	2.0	KACPRZAK_2022B_W211_NIRES						Huang et al. 2021	4.25640	-10.15330	
AGEL002527_-101107A	2.397	3.0	KACPRZAK_2020B_W127_NIRES	0.463 [*]			SDSS		Huang et al. 2021	6.36430	10.18530	
AGEL002700-041324A	1.465	2.0	KACPRZAK_2019B_W226_ESI	0.495 [*]					Jacobs et al. 2019a,b	6.75025	-4.22321	
AGEL003508-252658A				0.775	1.0	LOPEZ_105.20KF.001_XShooter			Jacobs et al. 2019a,b	8.78153	-25.44932	
AGEL003727-413150A	3.257	2.0	GLAZEBROOK_0101.A-0577_XShooter	0.708	3.0	GLAZEBROOK_0101.A-0577_XShooter			Jacobs et al. 2019a,b	9.36280	-41.53054	
AGEL004144-233905A	2.203	3.0	JELTEMA_2024B_U225_KCWI	0.439	3.0	JELTEMA_2024B_U225_KCWI			Huang et al. 2021	10.43410	-23.65150	
AGEL004257-371858A	3.094	3.0	LOPEZ_105.20KF.001_XShooter	0.883	2.0	LOPEZ_105.20KF.001_XShooter			Jacobs et al. 2019a,b	10.73881	-37.31623	
AGEL004827-031117A	2.367	2.0	JONES_2019B_U058_ESI	0.357 [*]			SDSS		Jacobs et al. 2019a,b	12.11340	3.18808	
AGEL010128-334319A	1.167	3.0	GLAZEBROOK_0101.A-0577_XShooter	0.581	2.0	GLAZEBROOK_0101.A-0577_XShooter			Jacobs et al. 2019a,b	15.36604	-37.22201	
AGEL010158-491738A	2.632	2.0	LOPEZ_108.223L.001_XShooter						Jacobs et al. 2019a,b	15.69182	-49.29394	
AGEL010238-015857A	1.816	2.0	JONES_2019B_U058_ESI	0.867	2.0	JONES_2019B_U058_ESI			Blake et al. 2016			
AGEL010257-291122A	0.815	3.0	LOPEZ_108.223L.001_XShooter	0.273 [*]					Jacobs et al. 2019a,b	15.73954	-29.18939	
AGEL011759-052718A	2.066	3.0	KACPRZAK_2020B_W127_NIRES	0.579	3.0	JONES_2019B_U058_ESI			Jacobs et al. 2019a,b	19.49477	-5.45492	
AGEL012429-291856A	1.606	3.0	LOPEZ_108.223L.001_XShooter						Jacobs et al. 2019a,b	21.11886	-29.31561	
AGEL012453-144303A	1.825	1.0	KACPRZAK_2020B_W127_NIRES	0.478	3.0	JONES_2019B_U058_ESI			Jacobs et al. 2019a,b	21.21019	-14.71738	
AGEL013003-374458A	2.282	3.0	LOPEZ_105.20KF.001_XShooter						Jacobs et al. 2019a,b	22.51201	-37.74938	
AGEL013355-643413A	2.093	3.0	LOPEZ_105.20KF.001_XShooter	0.326	3.0	LOPEZ_105.20KF.001_XShooter			Jacobs et al. 2019a,b	23.47773	-64.57028	
AGEL013442-043350A	1.568	3.0	KACPRZAK_2020B_W127_NIRES	0.551 [*]			SDSS		Jacobs et al. 2019a,b	24.56959	1.98243	
AGEL013442-043350B	2.031	3.0	KACPRZAK_2020B_W127_NIRES	0.551 [*]			SDSS		Jacobs et al. 2019a,b	24.63160	4.56390	
AGEL013639-000818A	2.629	3.0	JONES_2020B_U044_NIRES	0.344	3.0	JONES_2020B_U044_ESI			Jacobs et al. 2019a,b	24.16310	0.13836	
AGEL013719-083056A	2.997	3.0	JONES_2019B_U058_ESI	0.563	3.0	JONES_2019B_U058_ESI			Jacobs et al. 2019a,b	24.32850	-8.51552	
AGEL014106-171324A	2.436	3.0	JONES_2019B_U058_ESI	0.609	3.0	JONES_2019B_U058_ESI			Jacobs et al. 2019a,b	25.27558	-17.22326	
AGEL014235-164818A	2.309	3.0	KACPRZAK_2020B_W127_NIRES	0.619	2.0	JONES_2020B_U044_ESI			Jacobs et al. 2019a,b	25.64570	-16.80487	
AGEL014253-181316A	2.470	3.0	GLAZEBROOK_0101.A-0577_XShooter	0.637	3.0	GLAZEBROOK_0101.A-0577_XShooter			Jacobs et al. 2019a,b	25.72030	-18.52105	
AGEL014327-085021A	2.755	3.0	KACPRZAK_2020B_W127_NIRES	0.737	3.0	KACPRZAK_2019B_W226_ESI			Jacobs et al. 2019a,b	26.58622	-8.83925	
AGEL014504-045514A	1.960	3.0	JONES_2020B_U044_NIRES	0.635	3.0	JONES_2020B_U044_ESI			Jacobs et al. 2019a,b	26.26791	-4.93084	
AGEL014556-040229A	2.361	3.0	JONES_2020B_U044_NIRES	0.784	3.0	JONES_2020B_U044_ESI			Jacobs et al. 2019a,b	26.48478	4.04139	
AGEL015009-030438A	1.390	1.0	KACPRZAK_2020B_W127_NIRES						Huang et al. 2020	27.97230	-14.80690	
AGEL015153-144825A	2.258	3.0	KACPRZAK_2021B_W242_NIRES						Jacobs et al. 2019a,b	29.17803	-10.18339	
AGEL015643-101100A	2.486	3.0	KACPRZAK_2021B_W242_NIRES						Jacobs et al. 2019a,b	31.55611	-1.23817	
AGEL020613-011417A	1.303	3.0	JONES_2020B_U044_NIRES	0.714 [*]			SDSS		Jacobs et al. 2019a,b	31.77773	-27.44577	
AGEL020707-272645A	1.679	3.0	LOPEZ_105.20KF.001_XShooter						Jacobs et al. 2019a,b	31.77773	-27.44577	
AGEL020727-272645B	1.677	3.0	LOPEZ_105.20KF.001_XShooter						Jacobs et al. 2019a,b	41.52050	-6.12750	
AGEL021225-085211A	2.202	1.0	KACPRZAK_2020B_W127_NIRES	0.759 [*]			SDSS		Jacobs et al. 2019a,b	42.17181	-55.40325	
AGEL022709-471856A				0.603	3.0	GLAZEBROOK_0101.A-0577_XShooter			Jacobs et al. 2019a,b	36.37874	-47.31550	
AGEL022931-290816A	1.679	3.0	LOPEZ_105.20KF.001_XShooter	0.857	2.0	LOPEZ_105.20KF.001_XShooter			Jacobs et al. 2019a,b	37.37911	-29.13786	
AGEL023211-001339A	2.366	3.0	JONES_2020B_U044_NIRES	0.893	2.0	JONES_2020B_U044_ESI			Jacobs et al. 2019a,b	38.04683	0.22756	
AGEL024303-000600A	1.729	3.0	JONES_2020B_U044_NIRES	0.367 [*]			SDSS		Jacobs et al. 2019a,b	40.76267	-0.10005	
AGEL024303-000600B	2.806	2.0	KACPRZAK_2019B_W226_ESI	0.367 [*]			SDSS		Jacobs et al. 2019a,b	40.76267	-0.10005	
AGEL024605-060739A	2.730	3.0	KACPRZAK_2021B_W242_NIRES						Huang et al. 2020	41.52050	-6.12750	
AGEL025052-552412A	2.478	3.0	LOPEZ_105.20KF.001_XShooter	0.722	3.0	LOPEZ_105.20KF.001_XShooter			Jacobs et al. 2019a,b	42.17181	-55.40325	
AGEL025220-473283A				0.494	3.0	GLAZEBROOK_0101.A-0577_XShooter			Jacobs et al. 2019a,b	43.08284	-47.54382	
AGEL033203-132510A	2.335	3.0	KACPRZAK_2022B_W211_NIRES						Jacobs et al. 2019a,b	53.01064	-13.41950	
AGEL033717-315214A	1.955	3.0	GLAZEBROOK_0101.A-0577_XShooter	0.525	3.0	GLAZEBROOK_0101.A-0577_XShooter			Jacobs et al. 2019a,b	53.01064	-13.41950	
AGEL034131-513045A	2.035	2.0	LOPEZ_108.223L.001_XShooter						Jacobs et al. 2019a,b	53.52183	-31.87043	
AGEL035346-170639B	1.460	2.0	JONES_2021B_U013_KCWI	0.617	2.0	JONES_2021B_U013_KCWI			Jacobs et al. 2019a,b	55.57833	-51.51241	
AGEL035346-170639A	1.675	3.0	JONES_2021B_U013_KCWI	0.617	2.0	JONES_2021B_U044_ESI			Jacobs et al. 2019a,b	58.44268	-17.11090	
AGEL035418-160952A	1.910	1.0	KACPRZAK_2020B_W127_NIRES	0.574	3.0	GLAZEBROOK_0101.A-0577_XShooter			Jacobs et al. 2019a,b	58.57614	-16.14540	
AGEL040823-532714A	1.718	3.0	GLAZEBROOK_0101.A-0577_XShooter	0.564	3.0	GLAZEBROOK_0101.A-0577_XShooter			Diehl et al. 2017	62.09439	-53.45394	
AGEL042439-331742A	1.188	3.0	KACPRZAK_2021B_W242_NIRES	0.343	3.0	LOPEZ_105.20KF.001_XShooter			Jacobs et al. 2019a,b	66.16119	-33.29491	
AGEL043806-322852A	0.920	2.0	KACPRZAK_2021B_W242_NIRES	0.354	3.0	LOPEZ_108.223L.001_XShooter			Jacobs et al. 2019a,b	69.52327	-32.48116	
AGEL053724-464702A	2.344	2.0	LOPEZ_108.223L.001_XShooter	0.521	3.0	JONES_2020B_U044_ESI			Jacobs et al. 2019a,b	74.35165	-46.78401	
AGEL061815-501821A	2.336	3.0	JONES_2024A_U039_KCWI	0.722 [*]			SDSS		Jacobs et al. 2019a,b	74.56390	-30.30590	
AGEL075524-345404A	2.635	2.0	JONES_2020B_U044_NIRES	0.475 [*]			SDSS		Jacobs et al. 2019a,b	118.84800	34.76100	
AGEL080880-103142B	1.452	3.0	JONES_2020B_U044_ESI	0.475 [*]			SDSS		Jacobs et al. 2019a,b	122.08520	10.52840	
AGEL080880-103142A	1.303	3.0	JONES_2020B_U044_ESI	0.475 [*]			SDSS		Jacobs et al. 2019a,b	122.08520	10.52840	
AGEL0808930-021025A	1.769	3.0	KACPRZAK_2022B_W211_NIRES						Jacobs et al. 2019a,b	129.87662	2.17349	
AGEL0804633-031517A	2.635	2.0	KACPRZAK_2022B_W211_NIRES						Jacobs et al. 2019a,b	131.63169	-1.90446	
AGEL0804933-294328A	2.057	3.0	KACPRZAK_2022B_W211_NIRES	0.680 [*]			SDSS		Jacobs et al. 2019a,b	132.42941	29.72437	
AGEL085331-232155A	2.190	3.0	KACPRZAK_2021A_W235_NIRES	0.306		JONES_2021A_U022_ESI			Jacobs et al. 2019a,b	133.38000	23.36520	
AGEL085413-042400A	2.393	3.0	NANAYAKARA_2022A_W226_KCWI						Jacobs et al. 2019a,b	133.55308	-4.40257	
AGEL085917-061517A	2.658	3.0	KACPRZAK_2022B_W211_NIRES						Jacobs et al. 2019a,b	134.82065	6.25486	
AGEL0900115-095624A	2.637	3.0	KACPRZAK_2021B_W242_NIRES						Jacobs et al. 2019a,b	135.31250	9.94010	
AGEL091126-141757A	1.206	3.0	JONES_2021B_U012_ESI	0.546 [*]			SDSS		Jacobs et al. 2019a,b	137.85680	14.29910	
AGEL091905-033639A	2.193	3.0	KACPRZAK_2022B_W211_NIRES	0.444 [*]			SDSS		Jacobs et al. 2019a,b	139.76916	3.61072	
AGEL091935-303156A	1.812	3.0	KACPRZAK_2021A_W235_NIRES	0.427 [*]			SDSS		Jacobs et al. 2019a,b	139.89600	30.53230	
17307, Tran												

Table 4. Redshifts Measured as part of the AGEL Survey.(1) AGEL ID comprised of RA±DEC and the arc ID (A for main arc, B for second arc), (2) Source redshift, (3) Source redshift quality flag (3 high, 1 low), (4) Proposal ID for source redshift, (5) Deflector redshift, where a caret (^) indicates a literature measurement, (6) Deflector redshift quality flag (3 high, 1 low), (7) Proposal ID for source redshift, (8) Proposal ID and PI of HST photometry, (9) Origin of literature redshift measurement. (10) Right Ascension (11) Declination.

Object Name (1)	z_{source} (2)	Source flag (3)	Source Proposal ID (4)	$z_{\text{deflector}}$ (5)	Deflector flag (6)	Deflector Proposal ID (7)	HST Imaging (8)	Candidate Catalogue (9)	RA (10)	Dec (11)
AGEL092315+182943A	2.418	2.0	KACPRZAK_2021A_W235_NIRES	0.873 ⁻		SDSS	15867, Huang	Huang et al. 2020	140.81100	18.49540
AGEL093333+091919B	2.435	3.0	KACPRZAK_2021A_W235_NIRES	0.743 ⁻		SDSS		Jacobs et al. 2019a,b	143.38871	9.32193
AGEL093333+091919A	2.435	3.0	KACPRZAK_2021A_W235_NIRES	0.743 ⁻		SDSS		Jacobs et al. 2019a,b	143.38871	9.32193
AGEL094412+322039A	2.125	3.0	KACPRZAK_2022B_W211_NIRES	0.450 ⁻		SDSS		Jacobs et al. 2019a,b	145.86522	-1.91482
AGEL094412+322039A	2.828	3.0	KACPRZAK_2021A_W235_NIRES	0.595 ⁻		SDSS		Jacobs et al. 2019a,b	146.04930	32.34410
AGEL101807-000812A	1.740	2.0	KACPRZAK_2021B_W242_NIRES	0.372 ⁻		SDSS		Huang et al. 2020	154.53070	-0.13680
AGEL101847-012132A	1.432	3.0	JONES_2021A_U022_ESI	0.388 ⁻		SDSS		Jacobs et al. 2019a,b	154.69720	-1.35900
AGEL103027-064109A	1.583	3.0	KACPRZAK_2021A_W235_NIRES	0.468	3.0	JONES_2021A_U022_ESI		Jacobs et al. 2019a,b	157.61347	-6.68582
AGEL104041+185052A	0.879	3.0	JONES_2021A_U022_ESI	0.314 ⁻		SDSS		Huang et al. 2021	160.17160	18.84770
AGEL105100-055628A	1.940	1.0	KACPRZAK_2021B_W242_NIRES	0.250 ⁻		SDSS		Huang et al. 2020	160.23510	-1.06630
AGEL110154-060623A	1.674	3.0	BARONE_2023B_W372_KCWI	0.483	3.0	BARONE_2023B_W372_KCWI		Wittman et al. 2002	162.75076	-5.94108
AGEL110245+121111A	2.806	3.0	KACPRZAK_2021B_W242_NIRES	0.925	2.0	JONES_2022A_U028_ESI		Huang et al. 2021	165.47540	-6.04230
AGEL113929-021826A	1.553	3.0	KACPRZAK_2022B_W211_NIRES					Huang et al. 2020	165.68760	12.18640
AGEL114159+191815A	3.003	3.0	KACPRZAK_2022B_W211_NIRES	1.443 ⁻		SDSS		Jacobs et al. 2019a,b	174.87270	-2.30722
AGEL120535+411044A	2.658	3.0	JONES_2021B_U012_ESI	0.661	3.0	JONES_2021B_U012_ESI		Jacobs et al. 2019a,b	175.49611	19.30406
AGEL123809+150151A	1.161	3.0	JONES_2021A_U022_ESI	0.572	3.0	JONES_2021A_U022_ESI		Huang et al. 2021	181.39750	41.17900
AGEL125146+014256A	1.630	3.0	KACPRZAK_2021B_W242_NIRES	0.740	3.0	KACPRZAK_2021B_W242_NIRES		Jacobs et al. 2019a,b	189.53702	15.03090
AGEL123304+034319A	1.016	3.0	KIRBY_2021A_C250_MOSFIRE	0.353 ⁻		SDSS		Huang et al. 2021	192.94280	1.71550
AGEL133041+040401A	1.169	3.0	KACPRZAK_2021A_W235_NIRES	0.336 ⁻		SDSS		Jacobs et al. 2019a,b	200.76718	3.72207
AGEL133145+513431A	2.052	3.0	KACPRZAK_2021A_W235_NIRES	0.289 ⁻		SDSS		Huang et al. 2020	202.66900	4.67070
AGEL134333+415503B	2.843	3.0	JONES_2024A_U039_KCWI	0.418 ⁻				Huang et al. 2021	203.93880	51.57530
AGEL140839+251040A	1.289	2.0	JONES_2021A_U022_ESI	0.663 ⁻		SDSS		Stark et al. 2013	205.88689	41.91763
AGEL142104+002219A	2.208	3.0	KACPRZAK_2021B_W242_NIRES					Jacobs et al. 2019a,b	212.16144	25.51779
AGEL142719-064515A	1.513	3.0	KACPRZAK_2021A_W235_NIRES	0.265	3.0	JONES_2021A_U022_ESI		Huang et al. 2020	215.26540	0.37190
AGEL144133+005401A	1.667	3.0	NANAYAKKARA_2022A_W223_MOSFIRE	0.538 ⁻		SDSS		Jacobs et al. 2019a,b	216.82796	-7.57413
AGEL144149+144121B	2.340	3.0	NANAYAKKARA_2022A_W223_MOSFIRE	0.741 ⁻				Jacobs et al. 2019a,b	217.38753	-0.90039
AGEL150137+520830A	2.416	3.0	NANAYAKKARA_2022A_W223_MOSFIRE					Huang et al. 2021	220.45490	14.68910
AGEL150745+052256A	2.164	3.0	JONES_2020A_U160_NIRES	0.595 ⁻		SDSS		Huang et al. 2021	225.40500	52.14710
AGEL152560+052256B	2.591	3.0	JONES_2022A_U041_KCWI	0.595 ⁻		SDSS		Jacobs et al. 2019a,b	226.93811	5.38230
AGEL150925+390140A	1.523	3.0	JONES_2024A_U039_KCWI	0.682 ⁻		SDSS		Huang et al. 2021	227.35280	39.02790
AGEL152509+422753A	2.261	3.0	KACPRZAK_2021A_W235_NIRES					Huang et al. 2021	231.28740	42.46460
AGEL152560+084639A	1.951	3.0	JONES_2022A_U028_ESI	0.602 ⁻		SDSS		Jacobs et al. 2019a,b	231.49978	8.77744
AGEL153929+144324A	2.477	3.0	NANAYAKKARA_2022A_W223_MOSFIRE					Huang et al. 2021	234.47830	14.72320
AGEL153929+165016A	1.253	2.0	NANAYAKKARA_2022A_W223_MOSFIRE	0.410 ⁻		SDSS		Huang et al. 2021	234.87070	16.83790
AGEL155417+044339A	1.721	3.0	KACPRZAK_2020B_W127_NIRES	0.778	3.0	JONES_2022A_U028_ESI		Jacobs et al. 2019a,b	238.56911	4.72756
AGEL162300+213721A	1.728	3.0	KACPRZAK_2020B_W127_NIRES	0.758 ⁻		SDSS		Jacobs et al. 2019a,b	245.75139	21.62261
AGEL162401+012901A	2.367	3.0	NANAYAKKARA_2022A_W223_MOSFIRE	1.092 ⁻		JONES_2022A_U028_ESI		Huang et al. 2021	246.00620	1.48360
AGEL165140+280517A	2.376	3.0	JONES_2020B_U042_ESI					Huang et al. 2021	252.91730	28.08810
AGEL165742+344858A	2.465	3.0	JONES_2020B_U042_ESI					Huang et al. 2021	254.42350	34.81620
AGEL170944+315417A	2.119	2.0	NANAYAKKARA_2022A_W223_MOSFIRE					Huang et al. 2021	257.43480	31.90460
AGEL171922+244174A	2.279	3.0	KACPRZAK_2020B_W127_NIRES	0.529 ⁻		SDSS		Jacobs et al. 2019a,b	259.83059	24.68796
AGEL172703+110008A	1.337	3.0	JONES_2020B_U044_NIRES					Huang et al. 2019a,b	261.76369	11.02211
AGEL183520+460627A	3.392	3.0	KACPRZAK_2020B_W127_NIRES					Huang et al. 2021	278.83380	46.10760
AGEL193558+580909A	3.551	3.0	KACPRZAK_2020B_W127_NIRES	0.577	3.0	JONES_2020B_U044_ESI		Huang et al. 2021	293.99270	15.85250
AGEL20419+575701A	2.191	3.0	LOPEZ_105.20KF.001_XShooter	0.717	3.0	LOPEZ_105.20KF.001_XShooter		Jacobs et al. 2019a,b	303.58076	-57.95041
AGEL203412+060954A	1.892	3.0	KACPRZAK_2020B_W127_NIRES	0.791	3.0	JONES_2020B_U044_ESI		Huang et al. 2021	310.80200	-6.16490
AGEL205616+423857A				0.720	1.0	LOPEZ_105.20KF.001_XShooter		Jacobs et al. 2019a,b	314.06590	-42.64923
AGEL211005+563931A	1.182	3.0	LOPEZ_105.20KF.001_XShooter	0.500	3.0	LOPEZ_105.20KF.001_XShooter		Jacobs et al. 2019a,b	317.52247	-56.65849
AGEL211243+000921A	2.360	1.0	KACPRZAK_2022B_W211_NIRES	0.445 ⁻		SDSS		Jacobs et al. 2019a,b	318.17974	0.15577
AGEL211627-594702A	1.412	3.0	GLAZEBROOK_0101A-0577_XShooter	0.395	1.0	GLAZEBROOK_0101A-0577_XShooter		Jacobs et al. 2019a,b	319.11382	-59.78382
AGEL212252+005949A	0.928	3.0	JELTEMA_2024B_U225_KCWI	0.349	3.0	JELTEMA_2024B_U225_KCWI		Huang et al. 2021	320.71667	-0.99700
AGEL212326+015312A	1.180	3.0	JONES_2019B_U058_ESI	0.591 ⁻		SDSS		Huang et al. 2021	320.85840	1.88670
AGEL212512+650427A	2.223	2.0	GLAZEBROOK_0101A-0577_XShooter	0.779	3.0	GLAZEBROOK_0101A-0577_XShooter		Jacobs et al. 2019a,b	321.30012	-65.07408
AGEL213758+012924A	1.458	3.0	KACPRZAK_2019B_W226_ESI	0.273	3.0	KACPRZAK_2019B_W226_ESI		Jacobs et al. 2019a,b	322.49176	-4.18996
AGEL214915+001252A	1.945	3.0	JONES_2020B_U044_NIRES	0.453 ⁻		SDSS		Jacobs et al. 2019a,b	323.31380	-0.21431
AGEL215122+134718A	0.890	2.0	JONES_2020B_U044_ESI	0.206	3.0	JONES_2020B_U044_ESI		Huang et al. 2021	327.84080	13.78840
AGEL215844+025730A	2.081	3.0	KACPRZAK_2020B_W127_NIRES	0.287 ⁻		SDSS		Huang et al. 2021	329.68200	2.95840
AGEL221912+434854A	2.161	3.0	GLAZEBROOK_0101A-0577_XShooter	0.710	1.0	GLAZEBROOK_0101A-0577_XShooter		Jacobs et al. 2019a,b	334.80166	-43.80975
AGEL222609+004142A	1.896	3.0	JONES_2020B_U044_NIRES	0.647 ⁻		SDSS		Jacobs et al. 2019a,b	336.53876	0.69504
AGEL224405+275916A	0.960	3.0	JONES_2019B_U058_ESI	0.343 ⁻		SDSS		Huang et al. 2021	341.02060	27.98770
AGEL224621+223338A	2.257	3.0	JONES_2019B_U058_ESI					Stark et al. 2013	341.58817	22.56045
AGEL230305+511502A	2.568	3.0	LOPEZ_105.20KF.001_XShooter	0.514	3.0	LOPEZ_105.20KF.001_XShooter		Jacobs et al. 2019a,b	345.76962	-51.25050
AGEL230522+000212A	1.838	3.0	KACPRZAK_2019B_W226_ESI	0.492 ⁻		SDSS		Jacobs et al. 2019a,b	346.34025	-0.03655
AGEL231112+454658A	1.555	3.0	LOPEZ_105.20KF.001_XShooter	0.504	3.0	LOPEZ_105.20KF.001_XShooter		Jacobs et al. 2019a,b	347.79872	-45.78281
AGEL231812+110604A	2.656	2.0	KACPRZAK_2022B_W211_NIRES					Huang et al. 2020	349.54920	-11.10120
AGEL231935+115016A	1.990	3.0	JONES_2019B_U058_ESI	0.542	3.0	JONES_2019B_U058_ESI		Jacobs et al. 2019a,b	349.89385	11.83776
AGEL232128+463049A	1.749	2.0	LOPEZ_108.22JL.001_XShooter	0.701	2.0	LOPEZ_105.20KF.001_XShooter		Jacobs et al. 2019a,b	350.36821	-46.51371
AGEL233459+640407A	2.495	3.0	LOPEZ_105.20KF.001_XShooter	0.566	3.0	GLAZEBROOK_0101A-0577_XShooter		Jacobs et al. 2019a,b	353.74665	-64.06860
AGEL233552+515218A	2.225	3.0	GLAZEBROOK_0101A-0577_XShooter	0.494 ⁻		SDSS		Jacobs et al. 2019a,b	353.96636	-51.87161
AGEL233610+020735A	2.663	3.0	JONES_2020B_U044_NIRES	0.494 ⁻				Huang et al. 2021	354.04280	-2.12640
AGEL234930+511339A	1.393	2.0	LOPEZ_108.22JL.001_XShooter	0.430	3.0	JELTEMA_2023B_U039_NIRES		Jacobs et al. 2019a,b	357.37523	-51.22751
AGEL235934+020824A	1.119	3.0	JELTEMA_2023B_U039_NIRES					Huang et al. 2020	359.88970	2.13990

Table 5. Table 4 continued.

APPENDIX

Position (1)	Object Name (2)	HST Name (3)	RA (4)	Dec (5)
1	AGELO000316-334804A	DESJ0003-3348	0.81830	-33.80120
2	AGELO000645-442950A	DESJ0006-4429	1.68590	-44.49740
3	AGELO001310+004004A	DESJ0013+0040	3.29020	0.66770
4	AGELO004257-371858A	DESJ0042-3718	10.73880	-37.31620
5	AGELO10238+015857A	DESJ0102+0158	15.65960	1.98240
6	AGELO13355-643413A	DESJ0133-6434	23.47770	-64.57030
7	AGELO14106-171324A	DESJ0141-1713	25.27560	-17.22330
8	AGELO14253-183116A	DESJ0142-1831	25.72030	-18.52110
9	AGELO20613-011417A	DESJ0206-0114	31.55610	-1.23820
10	AGELO21225-085211A	DESJ0212-0852	33.10510	-8.86970
11	AGELO24303-000600A	DESJ0243-0006	40.76270	-0.10010
12	AGELO35346-170639A	DCLS0353-1706	58.44270	-17.11090
13	AGELO42439-331742A	DESJ0424-3317	66.16120	-33.29490
14	AGELO43806-322852A	DESJ0438-3228	69.52570	-32.48120
15	AGELO53724-464702A	DESJ0537-4647	84.35160	-46.78400
16	AGELO94412+322039A	DCLS0944+3220	146.04930	32.34410
17	AGEL132304+034319A	DCLS1323+0343	200.76720	3.72210
18	AGEL140839+253104A	DCLS1408+2531	212.16140	25.51780
19	AGEL142719-064515A	DCLS1427-0645	216.82800	-6.75410
20	AGEL150745+052256A	DCLS1507+0522	226.93810	5.38230
21	AGEL201419-575701A	DESJ2014-5757	303.58080	-57.95040
22	AGEL211005-563931A	DESJ2110-5639	317.52250	-56.65850
23	AGEL211243+000921A	DESJ2112+0009	318.17970	0.15580
24	AGEL211627-594702A	DESJ2116-5947	319.11380	-59.78380
25	AGEL212326+015312A	CSWA157	320.85840	1.88670
26	AGEL212512-650427A	DESJ2125-6504	321.30010	-65.07410
27	AGEL213758-012924A	DESJ2137-0129	324.49180	-1.49000
28	AGEL214915-001252A	DESJ2149-0012	327.31380	-0.21430
29	AGEL221912-434835A	DESJ2219-4348	334.80170	-43.80980
30	AGEL222609+004142A	DESJ2226+0041	336.53880	0.69500
31	AGEL224405+275916A	CSWA129	341.02060	27.98770
32	AGEL230305-511502A	DESJ2303-5115	345.76960	-51.25050
33	AGEL233459-640407A	DESJ2334-6404	353.74670	-64.06860
34	AGEL233552-515218A	DESJ2335-5152	353.96640	-51.87160
35	AGEL233610-020735A	PSJ1236	354.04280	-2.12640
36	AGELO000729-443446A	DESJ0007-4434	1.87200	-44.57950
37	AGEL010158-491738A	DESJ0101-4917	15.49180	-49.29390
38	AGEL012429-291856A	DESJ0124-2918	21.11890	-29.31560
39	AGELO22709-471856A	DESJ0227-4718	36.78730	-47.31550
40	AGELO25220-473238A	DESJ0252-4732	43.08280	-47.54380
41	AGELO33203-132510A	DCLS0332-1325	53.01060	-13.41950
42	AGELO34131-513045A	DESJ0341-5130	55.37830	-51.51240
43	AGELO40823-532714A	DESJ0408-5327	62.09440	-53.45390
44	AGELO85413-042409A	DCLS0854-0424	133.55310	-4.40260
45	AGELO90115+095624A	DESI-135.3125+09.9401	135.31250	9.94010
46	AGELO105100-055628A	DLS432021848	162.75080	-5.94110
47	AGEL172703+110008A	DCLS1727+1100	261.76370	11.00210
48	AGELO205616-423857A	DESJ2056-4238	314.06590	-42.64920
49	AGEL232128-463049A	DESJ2321-4630	350.36820	-46.51370
50	AGEL234930-511339A	DESJ2349-5113	357.37520	-51.22750
51	AGELO001030-431515A	DESJ0010-4315	2.62680	-43.25410
52	AGELO10520+014457A	DESJ0105+0144	16.33190	1.74900
53	AGELO21408-020629A	DCLS0214-0206	33.53340	-2.10790
54	AGELO24229-294305A	DESJ0242-2943	40.62050	-29.71820
55	AGELO25029-410418A	DESJ0250-4104	42.62080	-41.07170
56	AGELO30022-500129A	DESJ0300-5001	45.09020	-50.02470
57	AGELO32216-523440A	DESJ0322-5234	50.56840	-52.57790
58	AGELO32904-565658A	DESJ0329-5656	52.26620	-56.94940
59	AGELO35606-560729A	DESJ0356-5607	59.02600	-56.12480
60	AGELO41645-552500A	DESJ0416-5525	64.18670	-55.41680
61	AGELO42816-321800A	DESJ0428-3218	67.06770	-32.30000
62	AGELO53746-471120A	DESJ0537-4711	84.44090	-47.18900
63	AGELO600357-355806A	DESJ0603-3558	90.98540	-35.96830
64	AGELO132227-050135A	DCLS1322-0501	200.61330	-5.02630
65	AGEL144431+241843A	DCLS1444+2418	221.13010	24.31190
66	AGEL144640-000350A	DCLS1446-0003	221.66720	-0.06400
67	AGEL144743-065709A	DCLS1447-0657	221.92780	-6.95260
68	AGEL144802-081249A	DCLS1448-0812	222.00790	-8.21370
69	AGEL203911-545945A	DESJ2039-5459	309.79780	-54.99590
70	AGEL204555+003148A	DCLS2045+0031	311.47710	0.53000
71	AGEL212447-412816A	DESJ2124-4128	321.19660	-41.47100

Table A1. Object names for targets in Figure 3 (ID:16773, PI Glazebrook). (1) The subpanel position, counting from left to right, top to bottom. The colour reflects whether the object has both source and deflector redshifts (green), one of source or deflector redshift (orange), or no available redshifts (grey). (2) The AGELO object name. (3) The object name used in the HST observations. (4), (5) Right ascension and declination in decimal degrees.

Position (1)	Object Name (2)	HST Name (3)	RA	Dec
			(4)	(5)
1	AGEL212252-005949A	DES2122-0059	320.71667	-0.99700
2	AGEL091935+303156A	DLS210207	139.89600	30.53230
3	AGEL104041+185052A	DESI-160	160.17160	18.84770
4	AGEL014327-085021A	DESJ0143-0850	25.86222	-8.83925
5	AGEL023211+001339A	HSCJ023211+001339	38.04683	0.22756
6	AGEL011759-052718A	DESJ0117-0527	19.49477	-5.45492
7	AGEL014504-045551A	DESJ0145-0455	26.26791	-4.93084
8	AGEL013003-374458A	DES0130-3744	22.51201	-37.74938
9	AGEL053349-253654A	DESJ0533-2536	83.45553	-25.61511
10	AGEL103255+751854A	DESI-158.2306+75.3149	158.23060	75.31490
11	AGEL221638-441920A	DESJ2216-4419	334.15922	-44.32216
12	AGEL091433+301620A	DCLS0914+3016	138.63602	30.27227
13	AGEL085920+391702A	DESI-134.8336+39.2838	134.83363	39.28376
14	AGEL101103-001649A	DELJ101103-001649	152.76540	-0.28050
15	AGEL001030-431515A	DESJ0010-4315	2.62678	-43.25413
16	AGEL102643-023319A	DELJ102643-023319	156.67940	-2.55540
17	AGEL103858-354726A	DELJ103858-354726	159.74540	-35.79070
18	AGEL111800-153227A	DELJ111800-153227	169.50380	-15.54100
19	AGEL151048+630325A	DESI-227.7011+63.0570	227.70111	63.05703
20	AGEL082017+643112A	DESI-125.0716+64.5201	125.07158	64.52011
21	AGEL113521+714307A	DESI-173.8651+71.7367	173.86513	71.73673
22	AGEL224504-501725A	DESJ2245-5017	341.26572	-50.29037
23	AGEL212707-514951A	DESJ2127-5149	321.77933	-51.83083
24	AGEL110419-425746A	DELJ110419-425746	166.08090	-42.96280
25	AGEL012259-022705A	DES0122-0207	20.74568	-2.45147
26	AGEL225607+012534A	HSCJ225607+012534	344.03111	1.42638
27	AGEL210607-441154A	DESJ2106-4411	316.52989	-44.19821
28	AGEL165046+612939A	DESI-252.6907+61.4942	252.69066	61.49416
29	AGEL041810-545735A	DESJ0418-5457	64.54117	-54.95973
30	AGEL112354+505149A	DESI-171.0040+50.8683	171.00404	50.86830
31	AGEL170332+631417A	DESI-255.8840+63.2381	255.88400	63.23810
32	AGEL184141+741405A	DESI-280.4220+74.2348	280.42200	74.23480
33	AGEL015825-003959A	DES0158-0040	29.60320	-0.66649
34	AGEL042225-403156A	DESJ0422-4031	65.60553	-40.53217
35	AGEL035714-475647A	DES0357-4756	59.30752	-47.94633
36	AGEL014359+125610A	DCLS0143+1256	25.99491	12.93613
37	AGEL030416-492126A	DES0304-4921	46.06730	-49.35724
38	AGEL012441-015734A	DCLS0124-0157	21.17193	-1.95944
39	AGEL073726+665837A	DESI-114.3573+66.9769	114.35725	66.97694
40	AGEL005055-172033A	DCLS0050-1720	12.73022	-17.34243

Table A2. Object names for targets in 4 (ID:17307, PI Tran). (1) The subpanel position, counting from left to right, top to bottom. The colour reflects whether the object has both source and deflector redshifts (green), one of source or deflector redshift (orange), or no available redshifts (grey). (2) The AGEL object name. (3) The object name used in the HST observations. (4), (5) Right ascension and declination in decimal degrees.

Position (1)	Object Name (2)	HST Name (3)	RA (4)	Dec (5)
1	AGEL002527+101107A	DESI-006.3643+10.1853	6.36430	10.18530
2	AGEL013442+043350A	DESI-023.6765+04.5639	23.67650	4.56390
3	AGEL013639+000818A	DESI-024.1631+00.1384	24.16310	0.13836
4	AGEL061815+501821A	DESI-094.5639+50.3059	94.56390	50.30590
5	AGEL075524+344540A	DESI-118.8480+34.7610	118.84800	34.76100
6	AGEL080820+103142A	DESI-122.0852+10.5284	122.08520	10.52840
7	AGEL085331+232155A	DESI-133.3800+23.3652	133.38000	23.36520
8	AGEL092315+182943A	DESI-140.8110+18.4954	140.81100	18.49540
9	AGEL101807-000812A	DESI-154.5307-00.1368	154.53070	-0.13680
10	AGEL101847-012132A	DESI-154.6972-01.3590	154.69720	-1.35900
11	AGEL104056-010359A	DESI-160.2351-01.0663	160.23510	-1.06630
12	AGEL110154-060232A	DESI-165.4754-06.0423	165.47540	-6.04230
13	AGEL110245+121111A	DESI-165.6876+12.1864	165.68760	12.18640
14	AGEL120535+411044A	DESI-181.3974+41.1790	181.39750	41.17900
15	AGEL123809+150151A	DESI-189.5370+15.0309	189.53702	15.03090
16	AGEL125146+014256A	DESI-192.9428+01.7155	192.94280	1.71550
17	AGEL133041+044015A	DESI-202.6690+04.6707	202.66900	4.67070
18	AGEL133145+513431A	DESI-202.9388+51.5753	202.93880	51.57530
19	AGEL144133-005401A	DESI-220.3861-00.8995	220.38753	-0.90039
20	AGEL150925+390140A	DESI-227.3528+39.0279	227.35280	39.02790
21	AGEL153929+165016A	DESI-234.8707+16.8379	234.87070	16.83790
22	AGEL155417+044339A	DESI-238.5690+04.7276	238.56911	4.72756
23	AGEL162300+213721A	DESI-245.7514+21.6226	245.75139	21.62261
24	AGEL162401+012901A	DESI-246.0062+01.4836	246.00620	1.48360
25	AGEL171922+244117A	DESI-259.8396+24.6880	259.83959	24.68796
26	AGEL193558+580909A	DESI-293.9927+58.1525	293.99270	58.15250
27	AGEL204312-060954A	DESI-310.8019-06.1649	310.80200	-6.16490
28	AGEL215122+134718A	DESI-327.8408+13.7884	327.84080	13.78840
29	AGEL215844+025730A	DESI-329.6820+02.9584	329.68200	2.95840
30	AGEL001702-100911A	DESI-004.2564-10.1530	4.25640	-10.15300
31	AGEL142104+002219A	DESI-215.2654+00.3719	215.26540	0.37190
32	AGEL150137+520830A	DESI-225.4050+52.1417	225.40500	52.14170
33	AGEL152509+422753A	DESI-231.2858+42.4643	231.28740	42.46460
34	AGEL153755+144324A	DESI-234.4783+14.7232	234.47830	14.72320
35	AGEL165140+280517A	DESI-252.9173+28.0881	252.91730	28.08810
36	AGEL165742+344858A	DESI-254.4235+34.8162	254.42350	34.81620
37	AGEL170944+315417A	DESI-257.4348+31.9046	257.43480	31.90460
38	AGEL183520+460627A	DESI-278.8338+46.1076	278.83380	46.10760
39	AGEL231812-110604A	DESI-349.5492-11.1012	349.54920	-11.10120
40	AGEL013204-160014A	DESI-023.0157-16.0040	23.01570	-16.00400
41	AGEL014156+304531A	DESI-025.4848+30.7585	25.48480	30.75850
42	AGEL020145-273942A	DESI-030.4360-27.6618	30.43611	-27.66177
43	AGEL021514-290925A	DESI-033.8095-29.1570	33.80950	-29.15700
44	AGEL044821-192502A	DESI-072.0873-19.4172	72.08730	-19.41730
45	AGEL122537-072508A	DESI-186.4028-07.4188	186.40280	-7.41880
46	AGEL122719+172557A	DESI-186.8292+17.4324	186.82920	17.43240
47	AGEL123736+553343A	DESI-189.4008+55.5619	189.40080	55.56190
48	AGEL142749+081045A	DESI-216.9538+08.1792	216.95385	8.17917
49	AGEL144149+144121A	DESI-220.4549+14.6891	220.45490	14.68910
50	AGEL150511+172042A	DESI-226.2950+17.3451	226.29500	17.34510
51	AGEL151009+203725A	DESI-227.5364+20.6236	227.53640	20.62360

Table A3. Object names for targets in 5 (ID:15867, PI Huang). (1) The subpanel position, counting from left to right, top to bottom. The colour reflects whether the object has both source and deflector redshifts (green), one of source or deflector redshift (orange), or no available redshifts (grey). (2) The AGEL object name. (3) The object name used in the HST observations. (4), (5) Right ascension and declination in decimal degrees.

REFERENCES

- Abbott, T. M. C., Abdalla, F. B., Allam, S., et al. 2018, *ApJS*, 239, 18, doi: [10.3847/1538-4365/aae9f0](https://doi.org/10.3847/1538-4365/aae9f0)
- Alard, C. 2006, arXiv e-prints, astro, doi: [10.48550/arXiv.astro-ph/0606757](https://doi.org/10.48550/arXiv.astro-ph/0606757)
- Antwi-Danso, J., Papovich, C., Esdaile, J., et al. 2023, arXiv e-prints, arXiv:2307.09590, doi: [10.48550/arXiv.2307.09590](https://doi.org/10.48550/arXiv.2307.09590)
- Atek, H., Richard, J., Kneib, J.-P., et al. 2015, *ApJ*, 800, 18, doi: [10.1088/0004-637X/800/1/18](https://doi.org/10.1088/0004-637X/800/1/18)
- Barone, T. M., Kacprzak, G. G., Nightingale, J. W., et al. 2024, *Communications Physics*, 7, 286, doi: [10.1038/s42005-024-01778-4](https://doi.org/10.1038/s42005-024-01778-4)
- Bayer, D., Chatterjee, S., Koopmans, L. V. E., et al. 2023, *MNRAS*, 523, 1310, doi: [10.1093/mnras/stad1402](https://doi.org/10.1093/mnras/stad1402)
- Bayer, J., Huber, S., Vogl, C., et al. 2021, *A&A*, 653, A29, doi: [10.1051/0004-6361/202040169](https://doi.org/10.1051/0004-6361/202040169)
- Belokurov, V., Evans, N. W., Hewett, P. C., et al. 2009, *MNRAS*, 392, 104, doi: [10.1111/j.1365-2966.2008.14075.x](https://doi.org/10.1111/j.1365-2966.2008.14075.x)
- Belokurov, V., Evans, N. W., Moiseev, A., et al. 2007, *ApJL*, 671, L9, doi: [10.1086/524948](https://doi.org/10.1086/524948)
- Bergamini, P., Acebron, A., Grillo, C., et al. 2023, *ApJ*, 952, 84, doi: [10.3847/1538-4357/acd643](https://doi.org/10.3847/1538-4357/acd643)
- Biesiada, M., Piórkowska, A., & Malec, B. 2010, *MNRAS*, 406, 1055, doi: [10.1111/j.1365-2966.2010.16725.x](https://doi.org/10.1111/j.1365-2966.2010.16725.x)
- Blandford, R. D., & Narayan, R. 1992, *ARA&A*, 30, 311, doi: [10.1146/annurev.astro.30.1.311](https://doi.org/10.1146/annurev.astro.30.1.311)
- Bode, P., Ostriker, J. P., & Turok, N. 2001, *ApJ*, 556, 93, doi: [10.1086/321541](https://doi.org/10.1086/321541)
- Bolton, A. S., Burles, S., Koopmans, L. V. E., et al. 2008, *ApJ*, 682, 964, doi: [10.1086/589327](https://doi.org/10.1086/589327)
- Bolton, A. S., Brownstein, J. R., Kochanek, C. S., et al. 2012, *ApJ*, 757, 82, doi: [10.1088/0004-637X/757/1/82](https://doi.org/10.1088/0004-637X/757/1/82)
- Brownstein, J. R., Bolton, A. S., Schlegel, D. J., et al. 2012, *ApJ*, 744, 41, doi: [10.1088/0004-637X/744/1/41](https://doi.org/10.1088/0004-637X/744/1/41)
- Cañameras, R., Schuldt, S., Suyu, S. H., et al. 2020, *A&A*, 644, A163, doi: [10.1051/0004-6361/202038219](https://doi.org/10.1051/0004-6361/202038219)
- Cañameras, R., Schuldt, S., Shu, Y., et al. 2021, *A&A*, 653, L6, doi: [10.1051/0004-6361/202141758](https://doi.org/10.1051/0004-6361/202141758)
- Cabanac, R. A., Alard, C., Dantel-Fort, M., et al. 2007, *A&A*, 461, 813, doi: [10.1051/0004-6361:20065810](https://doi.org/10.1051/0004-6361:20065810)
- Caminha, G. B., Suyu, S. H., Grillo, C., & Rosati, P. 2022, *A&A*, 657, A83, doi: [10.1051/0004-6361/202141994](https://doi.org/10.1051/0004-6361/202141994)
- Chan, J. H. H., Wong, K. C., Ding, X., et al. 2024, *MNRAS*, 527, 6253, doi: [10.1093/mnras/stad2953](https://doi.org/10.1093/mnras/stad2953)
- Coe, D., Zitrin, A., Carrasco, M., et al. 2013, *ApJ*, 762, 32, doi: [10.1088/0004-637X/762/1/32](https://doi.org/10.1088/0004-637X/762/1/32)
- Collett, T. E. 2015, *ApJ*, 811, 20, doi: [10.1088/0004-637X/811/1/20](https://doi.org/10.1088/0004-637X/811/1/20)
- Collett, T. E., & Auger, M. W. 2014, *MNRAS*, 443, 969, doi: [10.1093/mnras/stu1190](https://doi.org/10.1093/mnras/stu1190)
- Collett, T. E., Auger, M. W., Belokurov, V., Marshall, P. J., & Hall, A. C. 2012, *MNRAS*, 424, 2864, doi: [10.1111/j.1365-2966.2012.21424.x](https://doi.org/10.1111/j.1365-2966.2012.21424.x)
- Collett, T. E., & Smith, R. J. 2020, *MNRAS*, 497, 1654, doi: [10.1093/mnras/staa1804](https://doi.org/10.1093/mnras/staa1804)
- Collett, T. E., Sonnenfeld, A., Frohmaier, C., et al. 2023, *The Messenger*, 190, 49, doi: [10.18727/0722-6691/5313](https://doi.org/10.18727/0722-6691/5313)
- Dey, A., Schlegel, D. J., Lang, D., et al. 2019, *AJ*, 157, 168, doi: [10.3847/1538-3881/ab089d](https://doi.org/10.3847/1538-3881/ab089d)
- Diehl, H. T., Buckley-Geer, E. J., Lindgren, K. A., et al. 2017, *ApJS*, 232, 15, doi: [10.3847/1538-4365/aa8667](https://doi.org/10.3847/1538-4365/aa8667)
- Drlica-Wagner, A., Carlin, J. L., Nidever, D. L., et al. 2021, *ApJS*, 256, 2, doi: [10.3847/1538-4365/ac079d](https://doi.org/10.3847/1538-4365/ac079d)
- Ebeling, H., Stockmann, M., Richard, J., et al. 2018, *ApJL*, 852, L7, doi: [10.3847/2041-8213/aa9fee](https://doi.org/10.3847/2041-8213/aa9fee)
- Eisenstein, D. J., Zehavi, I., Hogg, D. W., et al. 2005, *ApJ*, 633, 560, doi: [10.1086/466512](https://doi.org/10.1086/466512)
- Ferrami, G., & Wyithe, J. S. B. 2024, *MNRAS*, 532, 1832, doi: [10.1093/mnras/stae1607](https://doi.org/10.1093/mnras/stae1607)
- Florian, M. K., Rigby, J. R., Acharyya, A., et al. 2021, *ApJ*, 916, 50, doi: [10.3847/1538-4357/ac0257](https://doi.org/10.3847/1538-4357/ac0257)
- Gavazzi, R., Marshall, P. J., Treu, T., & Sonnenfeld, A. 2014, *ApJ*, 785, 144, doi: [10.1088/0004-637X/785/2/144](https://doi.org/10.1088/0004-637X/785/2/144)
- Gavazzi, R., Treu, T., Koopmans, L. V. E., et al. 2008, *ApJ*, 677, 1046, doi: [10.1086/529541](https://doi.org/10.1086/529541)
- Gavazzi, R., Treu, T., Marshall, P. J., Brault, F., & Ruff, A. 2012, *ApJ*, 761, 170, doi: [10.1088/0004-637X/761/2/170](https://doi.org/10.1088/0004-637X/761/2/170)
- Goobar, A., Mörtsell, E., Amanullah, R., & Nugent, P. 2002, *A&A*, 393, 25, doi: [10.1051/0004-6361:20020987](https://doi.org/10.1051/0004-6361:20020987)
- Hennawi, J. F., Gladders, M. D., Oguri, M., et al. 2008, *AJ*, 135, 664, doi: [10.1088/0004-6256/135/2/664](https://doi.org/10.1088/0004-6256/135/2/664)
- Hinton, S. R., Davis, T. M., Lidman, C., Glazebrook, K., & Lewis, G. F. 2016, *Astronomy and Computing*, 15, 61, doi: [10.1016/j.ascom.2016.03.001](https://doi.org/10.1016/j.ascom.2016.03.001)
- Huang, X., Storfer, C., Ravi, V., et al. 2020, *ApJ*, 894, 78, doi: [10.3847/1538-4357/ab7ffb](https://doi.org/10.3847/1538-4357/ab7ffb)
- Huang, X., Storfer, C., Gu, A., et al. 2021, *ApJ*, 909, 27, doi: [10.3847/1538-4357/abd62b](https://doi.org/10.3847/1538-4357/abd62b)
- Huang, X., Baltasar, S., Ratier-Werbin, N., et al. 2025, arXiv e-prints, arXiv:2502.03455, doi: [10.48550/arXiv.2502.03455](https://doi.org/10.48550/arXiv.2502.03455)
- Hughes, T. J., Glazebrook, K., & Jacobs, C. 2024, arXiv e-prints, arXiv:2403.04349, doi: [10.48550/arXiv.2403.04349](https://doi.org/10.48550/arXiv.2403.04349)
- Jacobs, C., Glazebrook, K., Collett, T., More, A., & McCarthy, C. 2017, *MNRAS*, 471, 167, doi: [10.1093/mnras/stx1492](https://doi.org/10.1093/mnras/stx1492)

- Jacobs, C., Collett, T., Glazebrook, K., et al. 2019a, MNRAS, 484, 5330, doi: [10.1093/mnras/stz272](https://doi.org/10.1093/mnras/stz272)
- . 2019b, ApJS, 243, 17, doi: [10.3847/1538-4365/ab26b6](https://doi.org/10.3847/1538-4365/ab26b6)
- Keerthi Vasan, G. C., Jones, T., Sanders, R. L., et al. 2023, ApJ, 959, 124, doi: [10.3847/1538-4357/acf462](https://doi.org/10.3847/1538-4357/acf462)
- Keerthi Vasan G., C., Jones, T., Shajib, A. J., et al. 2024, arXiv e-prints, arXiv:2402.00942, doi: [10.48550/arXiv.2402.00942](https://doi.org/10.48550/arXiv.2402.00942)
- Lagattuta, D. J., Richard, J., Ebeling, H., et al. 2023, arXiv e-prints, arXiv:2303.09568, doi: [10.48550/arXiv.2303.09568](https://doi.org/10.48550/arXiv.2303.09568)
- LeCun, Y., Boser, B., Denker, J. S., et al. 1989, Neural Computation, 1, 541, doi: [10.1162/neco.1989.1.4.541](https://doi.org/10.1162/neco.1989.1.4.541)
- Li, R., Napolitano, N. R., Tortora, C., et al. 2020, ApJ, 899, 30, doi: [10.3847/1538-4357/ab9dfa](https://doi.org/10.3847/1538-4357/ab9dfa)
- Lopez, S., Tejos, N., Barrientos, L. F., et al. 2020, MNRAS, 491, 4442, doi: [10.1093/mnras/stz3183](https://doi.org/10.1093/mnras/stz3183)
- McLean, I. S., Steidel, C. C., Epps, H. W., et al. 2012, in Society of Photo-Optical Instrumentation Engineers (SPIE) Conference Series, Vol. 8446, Ground-based and Airborne Instrumentation for Astronomy IV, ed. I. S. McLean, S. K. Ramsay, & H. Takami, 84460J, doi: [10.1117/12.924794](https://doi.org/10.1117/12.924794)
- McLeod, D. J., McLure, R. J., Dunlop, J. S., et al. 2015, MNRAS, 450, 3032, doi: [10.1093/mnras/stv780](https://doi.org/10.1093/mnras/stv780)
- Metcalf, R. B., Meneghetti, M., Avestruz, C., et al. 2019, A&A, 625, A119, doi: [10.1051/0004-6361/201832797](https://doi.org/10.1051/0004-6361/201832797)
- Modigliani, A., Goldoni, P., Royer, F., et al. 2010, in Society of Photo-Optical Instrumentation Engineers (SPIE) Conference Series, Vol. 7737, Observatory Operations: Strategies, Processes, and Systems III, ed. D. R. Silva, A. B. Peck, & B. T. Soifer, 773728, doi: [10.1117/12.857211](https://doi.org/10.1117/12.857211)
- More, A., Cabanac, R., More, S., et al. 2012, ApJ, 749, 38, doi: [10.1088/0004-637X/749/1/38](https://doi.org/10.1088/0004-637X/749/1/38)
- More, A., Suyu, S. H., Oguri, M., More, S., & Lee, C.-H. 2017, ApJL, 835, L25, doi: [10.3847/2041-8213/835/2/L25](https://doi.org/10.3847/2041-8213/835/2/L25)
- Morrissey, P., Matuszewski, M., Martin, D. C., et al. 2018, ApJ, 864, 93, doi: [10.3847/1538-4357/aad597](https://doi.org/10.3847/1538-4357/aad597)
- Mortensen, K., Keerthi Vasan, G. C., Jones, T., et al. 2021, ApJ, 914, 92, doi: [10.3847/1538-4357/abfa11](https://doi.org/10.3847/1538-4357/abfa11)
- Nanayakkara, T., Glazebrook, K., Kacprzak, G. G., et al. 2016, ApJ, 828, 21, doi: [10.3847/0004-637X/828/1/21](https://doi.org/10.3847/0004-637X/828/1/21)
- Nightingale, J. W., He, Q., Cao, X., et al. 2022, arXiv e-prints, arXiv:2209.10566. <https://arxiv.org/abs/2209.10566>
- O'Donnell, J. H., Wilkinson, R. D., Diehl, H. T., et al. 2022, ApJS, 259, 27, doi: [10.3847/1538-4365/ac470b](https://doi.org/10.3847/1538-4365/ac470b)
- Oser, L., Ostriker, J. P., Naab, T., Johansson, P. H., & Burkert, A. 2010, ApJ, 725, 2312, doi: [10.1088/0004-637X/725/2/2312](https://doi.org/10.1088/0004-637X/725/2/2312)
- Percival, W. J., Reid, B. A., Eisenstein, D. J., et al. 2010, MNRAS, 401, 2148, doi: [10.1111/j.1365-2966.2009.15812.x](https://doi.org/10.1111/j.1365-2966.2009.15812.x)
- Petrillo, C. E., Tortora, C., Chatterjee, S., et al. 2017, MNRAS, 472, 1129, doi: [10.1093/mnras/stx2052](https://doi.org/10.1093/mnras/stx2052)
- . 2019, MNRAS, 482, 807, doi: [10.1093/mnras/sty2683](https://doi.org/10.1093/mnras/sty2683)
- Price, S. H., Bezanson, R., Labbe, I., et al. 2024, arXiv e-prints, arXiv:2408.03920, doi: [10.48550/arXiv.2408.03920](https://doi.org/10.48550/arXiv.2408.03920)
- Prochaska, J. X., Hennawi, J., Cooke, R., et al. 2020, pypeit/PypeIt: Release 1.0.0, v1.0.0, Zenodo, doi: [10.5281/zenodo.3743493](https://doi.org/10.5281/zenodo.3743493)
- Prochaska, J. X., Hennawi, J. F., Westfall, K. B., et al. 2020, Journal of Open Source Software, 5, 2308, doi: [10.21105/joss.02308](https://doi.org/10.21105/joss.02308)
- Refsdal, S. 1964, MNRAS, 128, 307, doi: [10.1093/mnras/128.4.307](https://doi.org/10.1093/mnras/128.4.307)
- Remus, R.-S., Dolag, K., Naab, T., et al. 2017, MNRAS, 464, 3742, doi: [10.1093/mnras/stw2594](https://doi.org/10.1093/mnras/stw2594)
- Ritondale, E., Auger, M. W., Vegetti, S., & McKean, J. P. 2019, MNRAS, 482, 4744, doi: [10.1093/mnras/sty2833](https://doi.org/10.1093/mnras/sty2833)
- Ruff, A. J., Gavazzi, R., Marshall, P. J., et al. 2011, ApJ, 727, 96, doi: [10.1088/0004-637X/727/2/96](https://doi.org/10.1088/0004-637X/727/2/96)
- Sahu, N., Tran, K.-V., Suyu, S. H., et al. 2024, arXiv e-prints, arXiv:2405.15427. <https://arxiv.org/abs/2405.15427>
- Shajib, A. J., Glazebrook, K., Barone, T., et al. 2022, ApJ, 938, 141, doi: [10.3847/1538-4357/ac927b](https://doi.org/10.3847/1538-4357/ac927b)
- Sharon, K., Cerny, C., Rigby, J. R., et al. 2022, arXiv e-prints, arXiv:2207.05709, doi: [10.48550/arXiv.2207.05709](https://doi.org/10.48550/arXiv.2207.05709)
- Sharon, K., Bayliss, M. B., Dahle, H., et al. 2020, ApJS, 247, 12, doi: [10.3847/1538-4365/ab5f13](https://doi.org/10.3847/1538-4365/ab5f13)
- Sheinis, A. I., Bolte, M., Epps, H. W., et al. 2002, PASP, 114, 851, doi: [10.1086/341706](https://doi.org/10.1086/341706)
- Sheu, W., Cikota, A., Huang, X., et al. 2024, ApJ, 973, 3, doi: [10.3847/1538-4357/ad65d3](https://doi.org/10.3847/1538-4357/ad65d3)
- Shu, Y., Cañameras, R., Schuldt, S., et al. 2022, A&A, 662, A4, doi: [10.1051/0004-6361/202243203](https://doi.org/10.1051/0004-6361/202243203)
- Shu, Y., Bolton, A. S., Mao, S., et al. 2016a, ApJ, 833, 264, doi: [10.3847/1538-4357/833/2/264](https://doi.org/10.3847/1538-4357/833/2/264)
- Shu, Y., Bolton, A. S., Kochanek, C. S., et al. 2016b, ApJ, 824, 86, doi: [10.3847/0004-637X/824/2/86](https://doi.org/10.3847/0004-637X/824/2/86)
- Smith, R. J., & Collett, T. E. 2021, MNRAS, 505, 2136, doi: [10.1093/mnras/stab1399](https://doi.org/10.1093/mnras/stab1399)

- Sonnenfeld, A., Gavazzi, R., Suyu, S. H., Treu, T., & Marshall, P. J. 2013a, ApJ, 777, 97, doi: [10.1088/0004-637X/777/2/97](https://doi.org/10.1088/0004-637X/777/2/97)
- Sonnenfeld, A., Treu, T., Gavazzi, R., et al. 2013b, ApJ, 777, 98, doi: [10.1088/0004-637X/777/2/98](https://doi.org/10.1088/0004-637X/777/2/98)
- Sonnenfeld, A., Verma, A., More, A., et al. 2020, A&A, 642, A148, doi: [10.1051/0004-6361/202038067](https://doi.org/10.1051/0004-6361/202038067)
- Stark, D. P., Auger, M., Belokurov, V., et al. 2013, MNRAS, 436, 1040, doi: [10.1093/mnras/stt1624](https://doi.org/10.1093/mnras/stt1624)
- Stein, G., Blaum, J., Harrington, P., Medan, T., & Lukić, Z. 2022, ApJ, 932, 107, doi: [10.3847/1538-4357/ac6d63](https://doi.org/10.3847/1538-4357/ac6d63)
- Storfer, C., Huang, X., Gu, A., et al. 2022, arXiv e-prints, arXiv:2206.02764, doi: [10.48550/arXiv.2206.02764](https://doi.org/10.48550/arXiv.2206.02764)
- Sukay, E., Khullar, G., Gladders, M. D., et al. 2022, ApJ, 940, 42, doi: [10.3847/1538-4357/ac9974](https://doi.org/10.3847/1538-4357/ac9974)
- Suyu, S. H., Marshall, P. J., Auger, M. W., et al. 2010, ApJ, 711, 201, doi: [10.1088/0004-637X/711/1/201](https://doi.org/10.1088/0004-637X/711/1/201)
- Tomczak, A. R., Quadri, R. F., Tran, K.-V. H., et al. 2014, ApJ, 783, 85, doi: [10.1088/0004-637X/783/2/85](https://doi.org/10.1088/0004-637X/783/2/85)
- Tran, K.-V. H., Harshan, A., Glazebrook, K., et al. 2022, AJ, 164, 148, doi: [10.3847/1538-3881/ac7da2](https://doi.org/10.3847/1538-3881/ac7da2)
- Treu, T. 2010, ARA&A, 48, 87, doi: [10.1146/annurev-astro-081309-130924](https://doi.org/10.1146/annurev-astro-081309-130924)
- Vegetti, S., Lagattuta, D. J., McKean, J. P., et al. 2012, Nature, 481, 341, doi: [10.1038/nature10669](https://doi.org/10.1038/nature10669)
- Vernet, J., Dekker, H., D'Odorico, S., et al. 2011, A&A, 536, A105, doi: [10.1051/0004-6361/201117752](https://doi.org/10.1051/0004-6361/201117752)
- Wang, Y., Vogelsberger, M., Xu, D., et al. 2019, MNRAS, 490, 5722, doi: [10.1093/mnras/stz2907](https://doi.org/10.1093/mnras/stz2907)
- Wilson, J. C., Henderson, C. P., Herter, T. L., et al. 2004, in Society of Photo-Optical Instrumentation Engineers (SPIE) Conference Series, Vol. 5492, Ground-based Instrumentation for Astronomy, ed. A. F. M. Moorwood & M. Iye, 1295–1305, doi: [10.1117/12.550925](https://doi.org/10.1117/12.550925)
- Wong, K. C., Suyu, S. H., Chen, G. C. F., et al. 2020, MNRAS, 498, 1420, doi: [10.1093/mnras/stz3094](https://doi.org/10.1093/mnras/stz3094)
- York, D. G., Adelman, J., Anderson, John E., J., et al. 2000, AJ, 120, 1579, doi: [10.1086/301513](https://doi.org/10.1086/301513)
- Yuan, T. T., Kewley, L. J., Swinbank, A. M., & Richard, J. 2012, ApJ, 759, 66, doi: [10.1088/0004-637X/759/1/66](https://doi.org/10.1088/0004-637X/759/1/66)
- Zaborowski, E. A., Drlica-Wagner, A., Ashmead, F., et al. 2023, ApJ, 954, 68, doi: [10.3847/1538-4357/ace4ba](https://doi.org/10.3847/1538-4357/ace4ba)
- Zahedy, F. S., Chen, H.-W., Rauch, M., Wilson, M. L., & Zabludoff, A. 2016, MNRAS, 458, 2423, doi: [10.1093/mnras/stw484](https://doi.org/10.1093/mnras/stw484)
- Zheng, W., Postman, M., Zitrin, A., et al. 2012, Nature, 489, 406, doi: [10.1038/nature11446](https://doi.org/10.1038/nature11446)
- Zhuang, Z., Leethochawalit, N., Kirby, E. N., et al. 2023, ApJ, 948, 132, doi: [10.3847/1538-4357/acc79b](https://doi.org/10.3847/1538-4357/acc79b)